Dendrimer Functionalized Graphene Oxide for Selenium Removal

by

Wenda Xiao

A thesis submitted in partial fulfillment of the requirements for the degree of

Master of Science

in

Chemical Engineering

Department of Chemical and Materials Engineering
University of Alberta

Abstract

Selenium is an essential trace element nutrient for human life, but it can be extremely toxic if taken excess. Various adsorbents have been applied for the removal of selenium from water but performed poorly in the removal of Se (VI), which is more bioavailable and more difficult to remove. Herein, we reported a new method to prepare poly (amido amine) functionalized graphene oxide (PAMAM-GO) with different generations (GO-G0 to GO-G4). The resulting products were applied in selenium removal from simulated water, showing an increasing capacity with increasing generation. The 4^{th} generation of PAMAM-GO (GO-G4) shows a removal capacity of 60.9 mg g^{-1} in Se (IV) and 77.9 mg g^{-1} in Se (VI) at pH 6. The adsorption mechanism is attributed to the electrostatic interaction between selenium oxyanions and the adsorbents, proved by the effects of initial pH on removal capacity and zeta potential measurements.

Preface

The results of this thesis will be sent for publication to the *Carbon* as Xiao, W., Liu, Q., and Zeng, H., "Dendrimer Functionalized Graphene Oxide for Selenium Removal". I was responsible for the data collection and analysis as well as the manuscript composition. Zeng, H. contributed to manuscript edits. Liu, Q. was the supervisory author and was involved with concept formation and manuscript edits.

Acknowledgement

I would like to express my sincere gratitude and appreciation to my supervisors, Professor Qingxia (Chad) Liu and Professor Hongbo Zeng, for their support and guidance throughout my MSc study. Professor Liu has abundant industry experience. I had a better understanding of the project as well as safety at workplace under his guidance. Professor Zeng's personal charm and profound knowledge have great impact on me during the past two years. From my supervisors, I learned about the passion to a profession, as well as many valuable lessons which will be essential in my future career.

I would like to thank Dr. Jingyi Wang, who helped me in reviewing manuscripts and gave me many valuable advices. I would also thank my colleges, Dr. Bin Yan, Chen Shi, Han Lu, Haiming Wang, Jiawen Zhang, Jingsi Chen, Jun Huang, Junmeng Li, Lei Xie, Lin Li, Ling Zhang, Mingbo Zhang, Qiuyi Lu, Xin Cui, Yuechao Tang, Yuxi Liu and other group members for their encouragement and discussions which I benefit a lot from.

I would also express my appreciation to Dr. Anqiang He, Dr. Arno de Klerk, Dr. Guangcheng Chen, Dr. Shiraz Merali, Dr. Xin Zhang, Dr. XinSong Lin for their assistance in using equipment and instruments.

My thank to our research group's administrative assistant Ms. Patricia Siferd and Mr. Carl Corbett, for always being accommodating, resourceful, and supportive. Also thanks to Ms. Lily Laser for the kind office help.

The financial support from Natural Sciences and Engineering Research Council of Canada (NSERC) and Teck Resources Ltd. are acknowledged.

Finally, I dedicate this work to my parents, my other family members, and to all of my friends. Without their support, I wouldn't have reached this far.

Table of Contents

List of Tables

List of Figures

List of Symbols

q_e	Equilibrium concentration of pollutant in the solid phase
C_e	Equilibrium concentration of pollutant in the liquid phase
q_{max}	maximum amount of adsorption
b	Langmuir adsorption equilibrium constant
K_F	Freundlich constant in Freundlich adsorption model
n	Freundlich constant in Freundlich adsorption model
q	Adsorption amount
C_0	Initial Se (IV) or Se (VI) concentration
W	Adsorbent weight
V	total solution volume
$h\upsilon$	Energy of photon
KE	Electron kinetic energy
BE	Electron binding energy
φ_s	Spectrometer work function
d	Interlayer spacing in Bragg's equation
λ	Wavelength of X-ray in Bragg's equation

θ	Diffraction angle in Bragg's equation
m/z	mass to charge ratio

List of Abbreviations

APTES	3-Aminopropyltriethoxysilane
ATR	Attenuated total reflection
CNT	Carbon nanotube
DMF	Dimethylformamide
DMSO	Dimethyl sulfoxide
DRIFT	Diffuse reflectance infrared Fourier transform
EDA	Ethylenediamine
FTIR	Fourier Transform Infrared Spectroscopy
GO	Graphene oxide
ICP-MS	Inductively Coupled Plasma Mass Spectrometry
IR	Infrared spectroscopy
IX	Ion exchange
MA	Methylacrylate
MGO	Magnetic graphene oxide
PAMAM	Poly (amido amine)
PAMAM-GO	Dendrimer functionalized graphene oxide

PAMAM-MGO	Dendrimer functionalized magnetic graphene oxide
RGO	Reduced graphene oxide
RO	Reverse osmosis
SNR	Signal-to-noise ratio
SX	Solvent extraction
TEM	Transmission Electron Microscopy
TGA	Thermogravimetric analysis
XPS	X-ray photoelectron spectroscopy
XRD	X-ray diffraction

Chapter 1 Introduction

1.1 Background of Selenium Pollution and Methods for Selenium Removal from Water

Selenium is an essential trace element nutrient for human life, however, it can be extremely toxic if taken excess. An upper tolerable limit set for selenium intake is 400 μg day^{-1}.[1] Elemental selenium and most metallic selenides have relatively low toxicities because of their low bioavailability. However, selenate and selenite are very toxic, having an oxidant mode of action similar to that of arsenic trioxide. The chronic toxic dose of selenite for humans is about 2400 to 3000 mg of selenium per day for a long time.[2]

Selenium compounds are found naturally in ground waters, and in agricultural runoffs from the use of selenium containing insecticides and herbicides. In addition, selenium pollution to water systems can also be caused by leaching of selenium from coal fly ash, mining and crude oil processing.[3]

Selenium occurs in the environment with inorganic forms and organic forms, including selenide (Se^{2-}), amorphous or polymeric elemental selenium (Se^{0}), selenite (SeO_3^{2-}), selenate (SeO_4^{2-}), and organic Se. Selenite-containing minerals also exist but these minerals are rare (Table 1-1).

Table 1-1 Chemical forms of selenium in the environment

Oxidative state	Chemical forms
Se^{2-}	Selenide (Se^{2-}, HSe^-, H_2Se)
Se^0	Element selenium (Se^0)
Se^{4+}	Selenite (SeO_3^{2-}, $HSeO_3^-$, H_2SeO_3)
Se^{6+}	Selenate (SeO_4^{2-}, $HSeO_4^-$, H_2SeO_4)
Organic Se	Selenomethionine, selenocysteine
Selenite-containing minerals	Gypsum

Selenium is most commonly found as oxygenated anions (selenite and selenate) in aqueous environments, although several species of selenium are stable. The following figure adapted from Eh-pH diagram indicates that selenite exists as the single charged anion ($HSeO_3^-$) below pH 7 while as the double charged anion (SeO_3^{2-}) above pH 7. In the meanwhile, the higher valence selenium in aqueous environments, selenate, is presented as the double charged anion whenever the pH is larger than 2. In that sense, the pH of the water must be taken into account for the removal of selenium along with the forms that selenium is presented in the water. The result of this complexity is that both the speciation and the pH of the water must be taken into account when attempting to remediate the selenium. This was demonstrated in early studies focusing on coagulation filtration and lime softening, which concluded that neither approach was effective for complete selenium removal, but that they could be optimized with pH adjustments.[4]

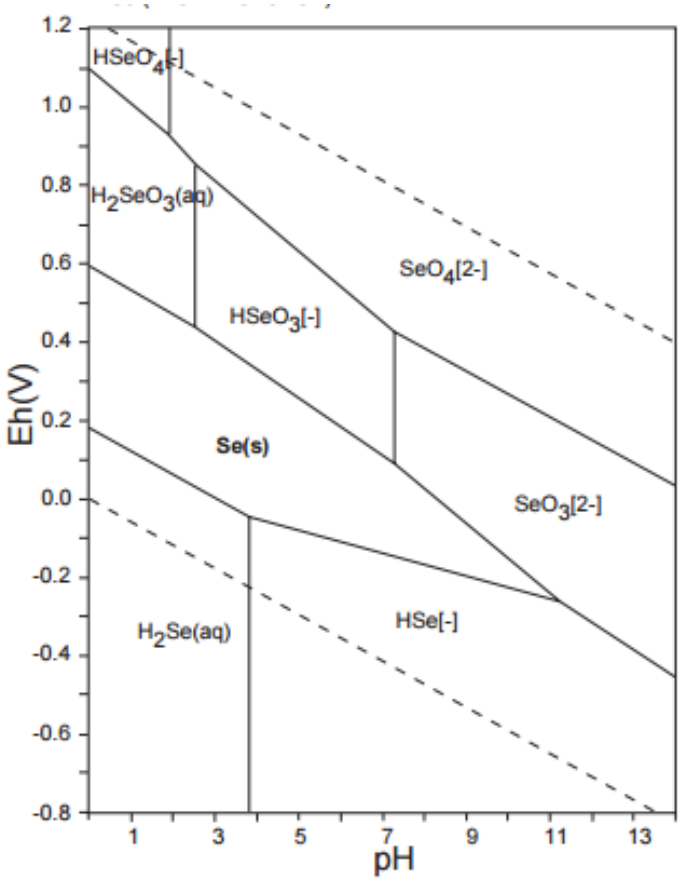

Figure 1-1 Eh-pH diagrams of the system Se-O-H. ΣSe = 10^{-10} mmol/g, 298.15K, 10^5 Pa.[5]

Due to increased enforcement of selenium regulations and an increased understanding of health and environmental effects, the need to be able to efficiently treat selenium has taken on an increased importance.[4] Researchers have applied various treatment technologies to remove selenium from water, including precipitation,[6-10] ion exchange (IX),[11] solvent extraction (SX),[12-13] reverse osmosis (RO),[14] emulsion liquid membrane,[15] nanofiltration,[16] reduction/oxidation[17] and adsorption.[18-23]

Among these methods, adsorption is an effective and economic way for waste water treatment. The adsorption process offers flexibility in design and operation and in many cases

will produce high-quality treated effluent. In addition, because physical adsorption is reversible, adsorbents can be regenerated by suitable desorption process.[24-25]

Table 1-2 Comparison of different methods for selenium removal.

Method for Se removal	Advantages and Disadvantages
Precipitation	Simple, economic, effective for selenite but ineffective for selenite, can cause secondary contamination due to disposal problems[24]
Ion Exchange	Effective for selenite, interfered by sulfate, problems with resin fouling and regeneration[26]
Solvent Extraction	High extraction ration in acid environment, problems with organic solvent after treatment[13]
Reverse Osmosis	Require extensive pretreatment, problems with membrane fouling[24]
Emulsion Liquid Membrane	Negative impact of sulfate on selenium removal[26]
Nanofiltration	Similar to RO but energy saving, operated at pressure[24]
Reduction	Time-consuming, expensive for some reagents[26]
Oxidation	Oxidizing agents are expensive[26]
Adsorption	Fast and easy, but highly interfered by other ions[24-26]

Various materials have been applied in waste water treatment as adsorbents, such as ash,[23] silica gel,[22] molecular sieves,[21] activated aluminum oxide,[20] activated carbon,[19] and meso-porous materials.[18] Most kinds of contaminants can be removed from water using adsorption process, including heavy metal ions and organic pollutants. Due to the increasing importance of

selenium remediation from waste water, several species of adsorbents including iron oxide, activated alumina, activated carbon and graphene oxide have been applied to remove selenium from waste water. However, most of these adsorbents perform well in Se (IV) removal but show poor performance in Se (VI) removal. Thus, a new kind of adsorbents that has higher adsorption capability, especially for Se (VI), needs to be designed and applied in selenium removal process.

1.2 Background of Dendrimers

First discovered and named by Tomalia and coworkers in 1985,[27] Dendrimers are a new class of polymeric materials. They are highly branched, monodisperse macromolecules. The structure of these materials has a great impact on their physical and chemical properties. As a result of their unique behavior, dendrimers are suitable for a wide range of biomedical and industrial applications.[28]

Dendrimers are mainly synthesized by two methods: divergent method and convergent method. In the divergent method, the dendrimer is assembled from a multifunctional core. The core molecule grows outwards by reactions with monomer molecules, typically by Michael addition reaction. Due to the occurrence of side reactions and incomplete reactions of the end groups which will lead to structure defects, large excess of reagents is required in the divergent method. It causes some difficulties in the purification of the final product.[27]

Compared to the divergent method, the convergent method was developed as an advantage to the divergent synthesis.[29] In the convergent method, dendrimers are built from small molecules, starting from the end groups and progressing inwards. The convergent approach has advantages including minimizing the possibility of failure sequences and avoiding large excesses of reagents, which simplifies the purification.[29]

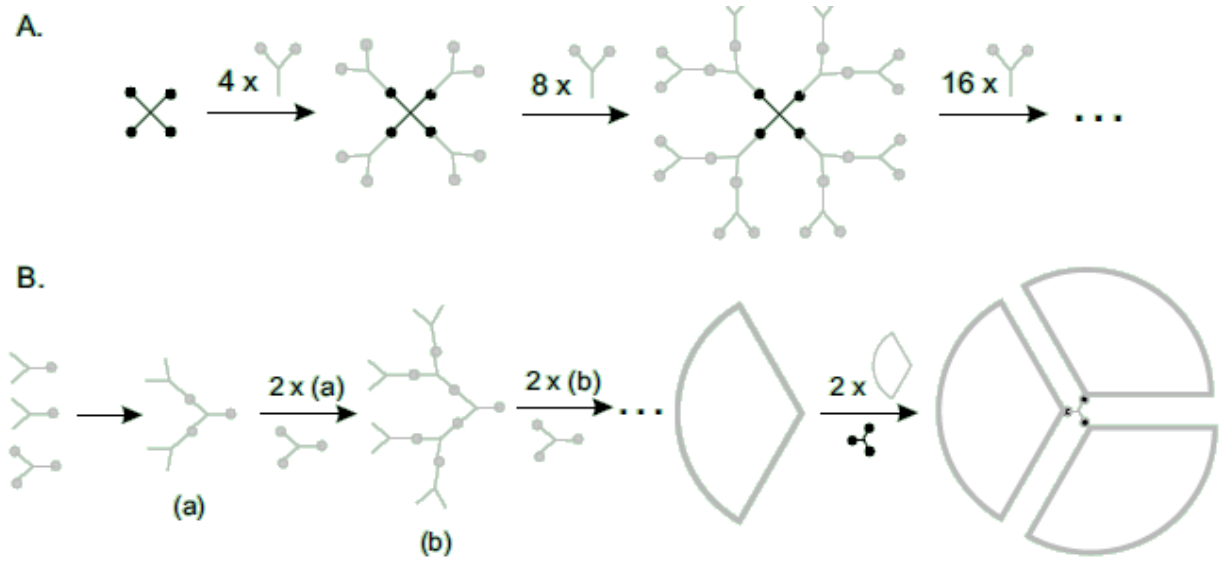

Figure 1-2 The divergent growth method (A) and the convergent growth method (B).[30]

The first dendrimer, poly (amido amine) (PAMAM), was made by Tomalia and coworkers, grown from a three-branched core prepared by reacting ammonia with methyl acrylate, followed by an excess of ethylenediamine.[27] This two-step sequence can be repeated to form successive generations, each with twice as many branches as the previous generation.[31] At the end of each branch is a free amino group, which has potential applications in biology[32-33] and chemistry.[34-38]

Acetylated PAMAM was prepared by reactions between PAMAM and acetic anhydride.[32] After acetylation of the outer layer, the dendrimer became water-soluble, and it was applied for the reduction of the toxicity of 5-Fluorouracil (5FU), as well as drug delivery. Dendrimers can also be applied as carriers in gene therapy. PAMAM can be used as a transfection reagent for the delivery of antisense oligonucleotides and plasmid expression vectors coding antisense mRNA.[33] And it was found that specific inhibition of targeted gene expression

with picomolar concentrations of specific oligonucleotides will occur when delivered by dendrimers.

Besides the applications in biology, PAMAM can also be applied in many chemical processes. The combination of large number of functional groups and high solubility makes dendrimers useful as nanoscale catalysts.[34] PAMAM encapsulated palladium (Pd) nanoparticles was prepared and applied as catalysts for the Heck reaction in 2001.[35] It was demonstrated that the nanocomposites are very efficient catalysts giving good yields under phosphine-free conditions and with 200 - 400 times less Pd than usual.

PAMAM has also been widely used as adsorbents, due to the large number of the functional groups. It was observed by Fadhel and co-workers that CO_2 adsorption capacities for the neat full generation PAMAM dendrimers were significantly enhanced by impregnation inside the pores of SBA-15 mesoporous substrate, which was attributed to the surface spreading of the dendrimers inside SBA-15, allowing accessibility of their amine groups to gaseous CO_2.[36] In another case, chitosan functionalized PAMAM was studied as adsorbents for Hg (II) removal, and the optimum pH for the removal process was found at 5.0.[37] Since magnetic separation has been considered as an effective method for solid-liquid phase separation, PAMAM-conjugated magnetic nanoparticles (Gn-MNPs) have also been investigated a lot. In 2010, Gn-MNPs were applied in the removal of Zn (II) from waste water.[38] It was found that more than 75% of the total G3-MNPs can be recovered after 10 consecutive cycles and the adsorption of Zn (II) was highly dependent on pH.

1.3 Graphene-Based Nanomaterials

1.3.1 Background of graphene and graphene oxide

Despite the short history, graphene has inspired huge interest in physics [39], materials science, chemistry and biology, following the study of C_{60}[40] and carbon nanotubes.[41] Graphene is defined as a flat monolayer of carbon atoms densely packed into a two-dimensional honeycomb lattice by Novoselov and his co-workers in 2004.[42] However, graphene is also defined as graphite with the layer number less than 10, which can be distinguished as three different types (single-, double- and few-).[43]

Graphene can also be regarded as a basic building block for graphitic materials of all other dimensionalities,[43] as depicted in the figure below. When graphene is wrapped up, it is known as 0D fullerenes (C_{60} or buckyball, molecule of carbon with 60 atoms, arranged similar to a soccer ball); when graphene is rolled, it can be 1D nanotubes (CNT, cylindrical wire-like structure with dimensions of a nanometer, can be single wall or multi-walls); when graphene is stacked with the number of layers larger than 10, it is known as 3D graphite.

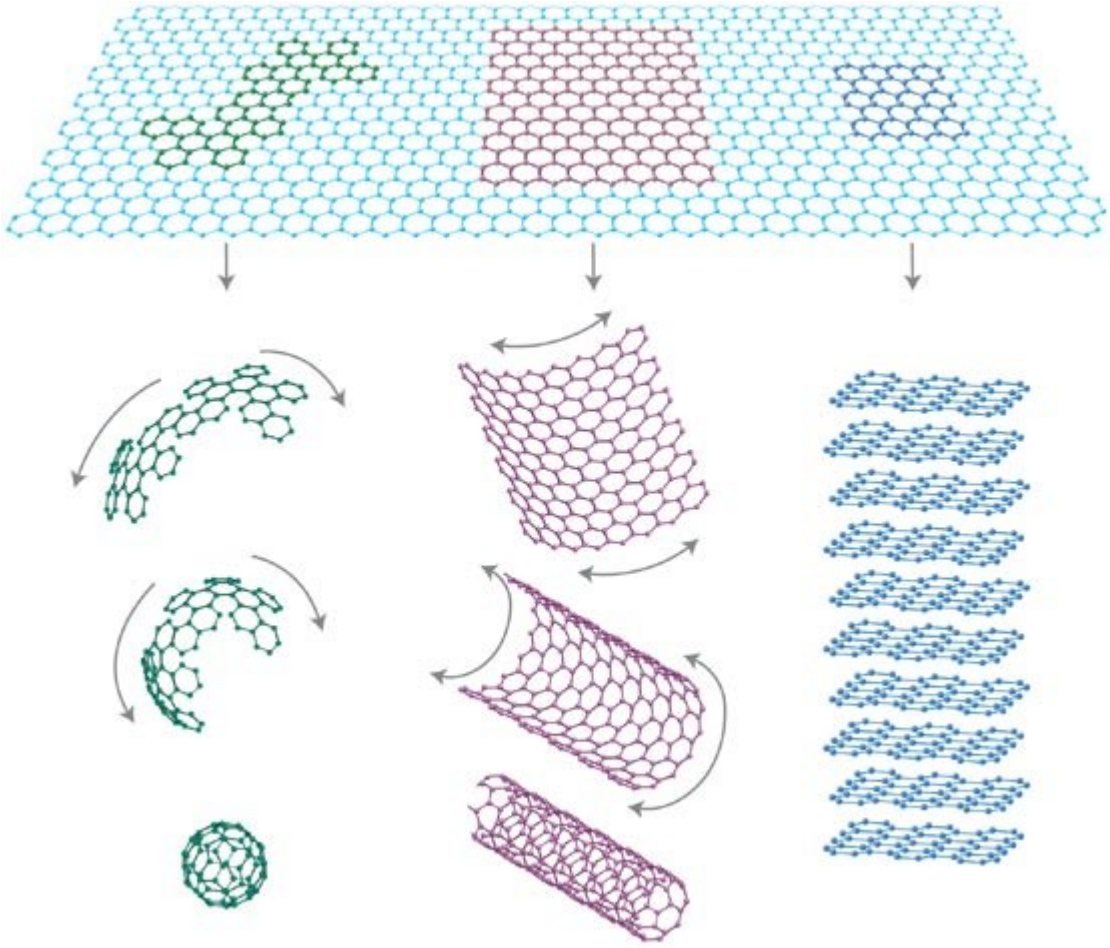

Figure 1-3 Mother of all graphitic forms. Graphene is a 2D building material for carbon material of all other dimensionalities. It can be wrapped up into 0D buckyballs, rolled into 1D nanotubes or stacked into 3D graphite.[43]

Since its successful preparation by mechanical cleavage from graphite in 2004[42], it has attracted large interest of researchers from different fields, due to its unique structure and many unusual characteristics. Graphene has a high theoretical surface area of 2965 m^2 g^{-1}.[44] Also, it possesses an outstanding Young's modulus (1060 GPa),[45] high electron mobility (15000 cm^2 $(V \cdot s)^{-1}$) at room temperature,[39] and other remarkable properties such as good quantum-tunnel effect and the half-integer quantum hall effect.[46-48]

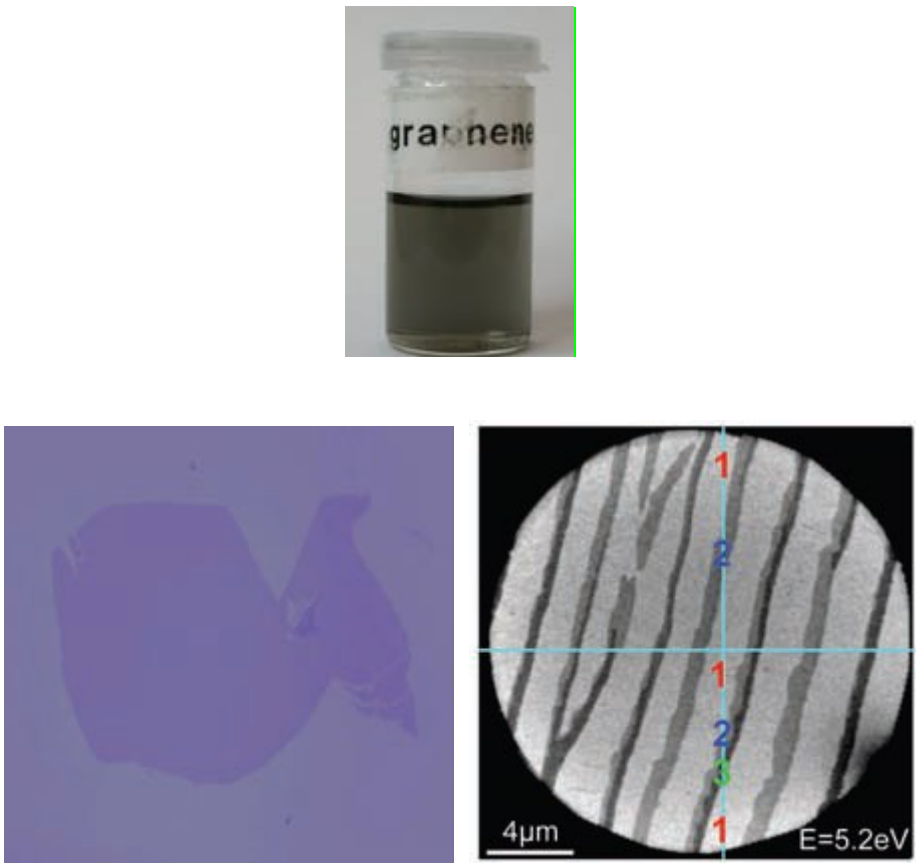

Figure 1-4 Making graphene: Suspension of microcrystals obtained by ultrasound cleavage of graphite in chloroform (top); large graphene crystal prepared on an oxidized Si wafer by the scotchtape technique (bottom left); state-of-the-art SiC wafer with atomic terraces covered by a graphitic monolayer (indicated by "1"), and double and triple layers ("2" and "3") (bottom right).[49]

Besides the mechanical cleavage method to make graphene, people use chemical process to obtain graphene as well, that is, to reduce graphene oxide. This process begins with the oxidation of natural graphite to make graphite oxide, before the preparation of graphene oxide by ultrasonic treatment of graphite oxide. After the reduction process, graphene oxide can be converted to graphene. The graphite oxide is typically formed by reacting graphite with strong

aqueous oxidizing agents. It was first prepared by Brodie in 1859, by treating graphite with a mixture of potassium chlorate and fuming nitric acid.[50] Later in 1898, Staudenmaier improved Brodie's method by adding the chlorate (such as $KClO_3$ or $NaClO_3$) in multiple aliquots during the reaction, as well as adding the concentrated sulfuric acid (H_2SO_4) to increase the acidity of the mixture.[51] In 1958, Hummers and Offeman developed a safer, quicker, and more efficient process using a mixture of sulfuric acid (H_2SO_4), sodium nitrate ($NaNO_3$) and potassium permanganate ($KMnO_4$).[52] The Hummers' method is still widely used, normally with some modifications. In general, the oxidation reaction could break the long-range p–p conjugation in the original graphite surface and result in the formation of sp^2 graphitic domains surrounded by disordered sp^3 oxidized domains with various oxygen-containing functional groups including hydroxyls (–OH), epoxides, carbonyls (–C=O), quinine, ketone, and phenol. The presence of these oxygen-containing functional groups reduces the interlayer forces and imparts strongly hydrophilic character, thereby facilitating the chemical processing of graphite oxide in solution and promoting the exfoliation of graphite oxide into individual sheets of GO in aqueous media via ultrasonic and stirring or rapid heating.

1.3.2 Functionalization of graphene and graphene oxide

As is known to all, graphene oxide possesses plentiful and reactive oxygen-containing functional groups, which are reactive sites for various chemical reactions and surface modifications. In general, there are three methods applied to the functionalization of graphene oxide, including surface transition metal adsorption, non-covalent functionalization and covalent functionalization.[53]

1.3.2.1 Transition metal adsorption

The hydroxyl groups and epoxy groups on the surface of graphene oxide provide active sites for anchoring metal ions. According to Wang and co-workers' work, Ti atoms could bind strongly to the oxygen sites with binding energies as high as 450 kJ mol^{-1}.[54] The Ti-anchored graphene oxide not only forms a stable motif but also acts as an excellent substrate for hydrogen storage. Besides Ti, Fe can also be anchored onto the surface of graphene oxide. The high-energy barrier of Fe atom diffusion on GO and the strong binding strength of Fe anchored on GO exclude the metal clustering problem and enhance the stability of the Fe-GO system. The Fe-anchored GO exhibits good catalytic activity for CO oxidation.[55]

1.3.2.2 Non-covalent functionalization

Non-covalent interaction is one of most frequently applied methods to prepare graphene nanocomposites. The interactions between organic molecules and graphene promote the attachment of organic species on graphene surfaces. Small molecules like surfactants and polymers can interact with graphene surfaces by π–π stacking, or electrostatic or hydrophobic interactions, which can provide useful ways to modify graphene surfaces for fabricating graphene nanocomposites.[56]

As one kind of small molecules, 1-pyrenebutyrate (PB^-) can be conveniently applied to modify graphene. A highly water-soluble graphene was obtained by functionalizing reduced graphene oxide with PB^-, though the strong p-stacking interactions between pyrene moiety in the molecule and graphene surfaces.[57] The obtained water-soluble graphene can be filtrated to fabricate large scale conductive graphene films with 7 orders of magnitude higher conductivity than graphene oxide. In another work, A novel graphene oxide-doxorubicin hydrochloride

nanohybrid (GO-DXR) was prepared via a simple non-covalent method, and the loading and release behaviors of DXR on GO were investigated.[58] The pH-dependent loading and releasing may be due to the hydrogen-bonding interactions between –OH and –COOH groups of graphene oxide and –OH and $–NH_2$ groups of DXR. At the same time, the fluorescence spectrum and electrochemical characterization results show that strong π-π stacking interactions exist between GO and DXR.

Along with small molecules, polymers are also widely applied to prepare functionalized graphene oxide by non-covalent interactions. Qi *et al.* prepared amphiphilic RGO sheets by using an amphiphilic coil-rod-coil conjugated triblock copolymer (PEG-OPE) as the π-π binding stabilizer.[59] The functionalized RGO forms a sandwich structure, which allows excellent solubility in a variety of solvents, including toluene and water. It was also found that amine-terminated polymers such as aminepolystyrene can be non-covalently attached to the carboxylate groups on graphene surfaces, and the nanocomposites showed high dispersibility in various organic media.[60]

1.3.2.3 Covalent functionalization

Covalent reaction is another method applied for the functionalization of graphene oxide, involving the reaction of functional molecules and the oxygenated groups on graphene oxide. The carboxylic groups at the edge of GO provide active sites for amidation and esterification.[61-63] Stankovich et al. reported graphene oxide attached to organic isocyanate via forming amides and carbamate esters with carboxyl and hydroxyl groups on the surfaces of graphene oxide, respectively.[61] Similarly, few-layer graphene materials were covalently functionalized with poly (vinyl alcohol) via ester linkages, and the resulting functionalized sample could be readily

soluble in aqueous and polar organic solvents, allowing solution-phase processing for various purposes such as the fabrication of polymer–carbon nanosheets composites containing no dispersion agents or any other foreign substances.[62]

The epoxy and hydroxyl groups can also be involved in reactions. The epoxy groups on the basal plane can be modified by nucleophilic ring-opening reactions, and the hydroxyl groups can be modified by reactions such as forming esters. Recently, polydisperse graphene nanosheets were synthesized and stabilized by the attachment of amine-terminated ionic liquid onto the basal plane of graphene oxide through ring-opening reaction with the epoxy groups.[64] The resulting graphene sheets can be stably dispersed in water, DMF, and DMSO without any assistance from polymeric or surfactant stabilizers. In another work, epoxy composites with both GO and silane-functionalized GO at different loadings have been prepared, and the resulting materials showed significant improvement of thermal and mechanical properties, due to silane covalent functionalization of GO that produces improved dispersion of GO and strong interfacial interaction with the epoxy matrix.[65]

1.3.3 Applications of graphene-based materials

1.3.3.1 Energy applications

Functionalized graphene nanocomposites have been intensively investigated for energy-related applications such as field-effect transistors (FET),[42, 66] photovoltaic devices, and sensor platforms. The first graphene-based FET was reported by Novoselov *et al.* in 2004.[42] The graphene films were prepared by mechanical exfoliation of small mesas of highly oriented pyrolytic graphite, and the as-prepared few-layer graphene had the sizes up to 10 μm. A top-gated graphene field-effect transistor (GFET) was designed based on a high-κ gate dielectric

without bandgap engineering.[66] The saturation velocity depends on the charge-carrier concentration, which was attributed to scattering by interfacial phonons in the SiO_2 layer supporting the graphene channels.

1.3.3.2 Graphene-based photocatalysis

During the past few years, photocatalytic decontamination has been intensively studied in many areas, particularly the treatment of environmental pollutants. Apart from some unique properties such as the large theoretical specific surface area and the high transparency due to its one-atom thickness, the exceptional electrical conductivity enables graphene to absorb visible light in addition to ultraviolet (UV) light. Because of the large two-dimensional surface size and the large structure of π–π conjugation, graphene nanosheets can act as both adsorbents and electron acceptors. Under light irradiation, the photoexcited electrons could be injected directly or from the nano photocatalytic material into the graphene nanosheets (or graphene oxide nanosheets). The synergistic effects between graphene nanosheets (or graphene oxide nanosheets) and the loaded photocatalytic materials make significant contributions to the obtained high photocatalytic activity. As a result, the injected electrons can easily move throughout each sheet of graphene nanosheets (or graphene oxide nanosheets), and the bandgap energy (Eg) would be reduced.[67] CdS nanorods/reduced graphene oxide (RGO) composites were fabricated through a facile one-pot hydrothermal synthesis.[68] The sample CdS/RGO-1% possesses excellent photocatalytic properties under visible light for the degradation of methyl orange with a rate constant of 1.76×10^{-2} min^{-1}, which is about three times higher than that of pure CdS nanorods. The novel composite material can also be used as an enzyme-free biosensor for H_2O_2 based on its electrocatalytic behaviour. The low-cost sensor shows rapid response and high sensitivity.

This method opens up a facile route for preparing graphene-based nanocomposites with excellent photocatalytic and electrocatalytic properties.[68] In another work, The Cu_2O/SnO_2/graphene (CSG) and SnO_2/graphene (SG) nanocomposite photocatalysts were prepared by simple sol-gel growth method, the resulting hybrid material SG showed superior photocatalytic activity to pure SnO_2 and graphene. And the greater photocatalytic activity of CSG indicated that Cu_2O addition could promote the photodegradation of pendimethalin at SG with favoring the transfer of light-induced electrons and holes between Cu_2O and SnO_2.[69]

TiO_2-based materials have been the most promising candidates for photocatalytic decontamination.[70] Zhang and co-worker prepared a chemically bonded TiO_2 (P25)-graphene nanocomposite photocatalyst with graphene oxide and P25, using a facile one-step hydrothermal method.[71] The as-prepared P25-graphene photocatalyst possessed great adsorptivity of dyes, extended light absorption range, and efficient charge separation properties simultaneously. It showed significant advancement over bare P25 in the photodegradation of MB dye under both UV and visible light irradiation.

1.3.3.3 Graphene-based materials as adsorbents

Due to its excellent properties such as large specific area, graphene and its derivatives have been examined for pollution management, including gas adsorption,[72-77] organic pollutants removal[78-80] and metal ions removal.[81-88]

The capacity of an adsorbent can be described by the equilibrium adsorption isotherm, which is characterized by certain constants whose values express the surface properties and affinity of the adsorbent. The adsorption isotherm is important from both theoretical and practical points of view. The parameters obtained from the different models provide important

information about the adsorption mechanism, the surface properties and the affinities of adsorbents.[72] Among the isotherm equations available for analyzing experimental adsorption equilibrium data, the most widely used adsorption models for single-solute systems are the Freundlich and Langmuir models. The Freundlich isotherm is expressed as follows:[89]

$$q_e = K_F C_e^{1/n} \tag{1-1}$$

The saturated monolayer isotherm (Langmuir equation) is represented as follows:[90]

$$q_e = \frac{q_{\max} b C_e}{1 + b C_e} \tag{1-2}$$

where q_e (mg g^{-1}) is the equilibrium concentration of pollutant in the solid phase; K_F ($mg^{1-1/n}\,L^{1/n}/g$) is the Freundlich constant representing the adsorption capacity; C_e (mg L^{-1}) is the equilibrium concentration of pollutant in the liquid phase; n is the constant describing the adsorption intensity; q_{max} (mg g^{-1}) is the maximum amount of adsorption; b (L mg^{-1}) is the Langmuir adsorption equilibrium constant.

Experimental studies of NH_3 adsorption/desorption on graphene surfaces were reported in 2009.[73] The study employed bottom-gated graphene field effect transistors supported on Si/SiO_2 substrates, and found that the molecules adsorbed and desorbed rapidly on the outer surface of the graphene, and much more slowly from the inner surface that is in contact with the SiO_2 gate dielectric. Several studies relevant to the mechanism of gas adsorption have been studied, such as H_2S adsorption on a graphene layer,[74] high-pressure CH_4 and CO_2 storage capacities,[2, 75] oxygen migration on graphene surface,[76] and gas adsorption on graphene doped with different atoms.[77]

The applications of graphene oxide and its derivatives in organic pollutants removal have been intensively studied due to the increasing environment pollution caused by organic compounds. Organic compounds can be adsorbed on nanoparticles or nanostructured materials via non-covalent interaction including electrostatic interaction, hydrogen bonds, π- π stacking, dispersion forces, dative bonds, and the hydrophobic effect.[91] In the case of graphene, the very large delocalized π-electron system plays the dominant role in the formation of strong π-π stacking interaction with the aromatic rings of several organic compounds,[92] while graphene oxide provides rich functional groups for the formation of hydrogen bonding or electrostatic interaction with organic compounds containing oxgen- and nitrogen-functional groups.[92]

Due to raising concerns over pollution of antibiotics including tetracyclines in aquatic environments in recent years, graphene oxide was used as an adsorbent for tetracycline antibiotics' removal from the aqueous solution owing to its excellent hydrophilicity, special structure, and high surface area. The mechanism for the adsorption of tetracycline on graphene oxide was deduced to be via π–π interaction and cation–π bonding.[78] In another work, Pei *et al.* investigated adsorption of 1,2,4-trichlorobenzene (TCB), 2,4,6-trichlorophenol (TCP), 2-naphthol and naphthalene (NAPH) on graphene (G) and graphene oxide (GO).[79] It was indicated that except for hydrophobic interaction, four aromatics were adsorbed on G mainly via π–π interaction. Compared to G, GO has lesser π-electron density and more O-containing functional groups and the higher adsorption of hydroxyl-substituted TCP and 2-naphthol on GO was mainly attributed to the formation of H-bonding between hydroxyl groups of TCP and 2-naphthol and O-containing functional groups on GO. Magnetic cyclodextrin–chitosan/graphene oxide (CCGO) with high surface area was synthesized via a simple chemical bonding method and examined for the removal of hydroquinone from simulated water in 2013.[80] The results indicated that

electrostatic interaction may not have a great influence on the adsorption, while the hydrogen bonds forming between hydroquinone and the hydroxyl/carboxyl groups on the CCGO may greatly influence the adsorption. Hydroquinone may be adsorbed by cavities of the cyclodextrin as well.

Although graphene can be applied as an ideal adsorbent for organic compounds because of the large π-electron system, it does not work so well in metal ions removal. The adsorption of metal ions therefore requires the formation of hydrophobic complexes.[92-93] However, graphene oxide is suitable for this situation due to its functional groups containing oxygen atoms which can form a metal complex with metal ions. The adsorption capacities of graphene oxide on organic compounds and metal ions are shown in Table 1-3. In general, the capacities of graphene oxide and its derivatives are higher than any other reported adsorbents. For instance, Ren and co-workers carried out a comparative study of Cu(II) decontamination by graphene oxide, multiwalled carbon nanotubes, and active carbon.[81] It was found that under acid conditions, GO has the highest adsorption efficiency with a maximum adsorption capacity of 1.18×10^{-3} mol g^{-1}. The adsorption of metal ions on GO is usually independent on the ionic strength, but highly dependent on the solution pH.[82-83]

Due to the very large specific surface area, graphene and graphene oxide are widely used to form nanocomposites as carriers. *N*-(trimethoxysilylpropyl) ethylenediamine triacetic acid (EDTA-silane) modified graphene oxide was prepared and it was found that the introduction of EDTA groups to the GO surface through silanization process can significantly increase the adsorption capacity of GO for heavy metal removal.[84] Also, the poly (*N*-vinylcarbazole) blended GO (PVK-GO) nanocomposite exhibits an exceptional adsorption capacity of Pb^{2+} in aqueous

solution, the adsorption capacity was directly influenced by the pH of the solution and increased with the concentration of graphene oxide in the PVK-GO nanocomposite.[85]

Magnetite/graphene composites are another promising adsorbent widely used in the preconcentration or separation of heavy metal ions from aqueous solutions.[67] They can be quickly separated and recovered from aqueous solution by an easy magnetic separation method. A magnetite/graphene oxide (M/GO) composite was synthesized via a chemical reaction with a magnetite particle size of 10-15 nm and was developed for the removal of heavy metal ions from aqueous solutions in 2011.[86] The sorption mechanism of Co (II) was attributed to inner-sphere surface complexation at low pH, while the removal was accomplished by simultaneous precipitation and inner-sphere surface complexation at high pH values. The magnetic graphene oxide can also be used for anions removal from waste water. The magnetic graphene oxide (MGO) composites were prepared by coprecipitation of $FeCl_3 \cdot 6H_2O$ and $FeCl_2 \cdot 4H_2O$ on graphene oxide (GO) nanosheets and applied to the removal of As (V) from aqueous solutions by Sheng and coworkers.[87] It was found that the MGO composites are very suitable materials for the removal of As (V) from aqueous solution in natural environmental pollution cleanup. In another case, the magnetic chitosan grafted graphene oxide (MCGO), which showed an increased surface area, was synthesized via a facile and fast process and further was developed to be highly efficient adsorbent for Pb^{2+} in aqueous solution.[88]

Table 1-3 The maximum absorption capacities of RGO, GO and their derivatives or composites toward organic compounds and metal ions.[92]

Adsorbate	Adsorbent	pH	MAC[a] mg g^{-1}	Adsorbate	Adsorbent	pH	MAC[a] mg g^{-1}
Tetracycline	GO	3.6	313	Cr(VI)	GO	3	65
Oxytetracycline	GO	3.6	212		GO/Fe_3O_4/β-CD	3	120
Doxycycline	GO	3.6	398	As(III)	RGO/Fe_3O_4	7	10-13
1-Naphthylamine	RGO/Fe_3O_4	7	408		RGO/Fe_3O_4/ MnO_2	7	14
1-Naphthol	RGO/Fe_3O_4	7	389	As(V)	RGO/Fe_3O_4	7	5.3-5.8
Naphthalene	RGO/Fe_3O_4	7	337		RGO/Fe_3O_4/ MnO_2	7	12
MB	GO	6	714	Cd(II)	GO	6	106
	GO	6	244		GO	5	345
	GO/chitosan/Fe_3O_4	10	181	Pb(II)	GO	6	842
Fuchsie	RGO/Fe_3O_4	6.6	89		GO	5	1119
Methyl orange	G/$CoFe_2O_4$	8	72		GO	6.8	328
Co(II)	GO	6	68		EDTA-GO	6.8	479
	GO/Fe_3O_4	6.8	13		RGO/MnO_2	6	180
Ni(II)	RGO	7	3		GO/Fe_3O_4/chitosan	5	77
	RGO/MnO_2	7	47	Au(III)	GO	5	146
Cu(II)	GO	5	47		GO/chitosan	4	1077
	GO	5	294	Pd(II)	GO	5	98
	GO	5.3	118		GO/chitosan	3	217
	GO	5.3	22	U(VI)	GO	5	98
	GO/Fe_3O_4	5.3	18		GO	4	299
	RGO/MnO_2	6	103		RGO	4	47
Zn(II)	GO	5	345	Eu(III)	GO	6	175

1.4 Design and Scope

This work combines the advantages of graphene oxide with poly (amido amine) to synthesize dendrimer-functionalized graphene oxide (PAMAM-GO). Graphene oxide has large surface area and abundant surface functional groups, providing active sites for adsorption and surface modification. Amine-terminated poly (amido amine) exhibits high affinity with high valence selenium oxyanions, which can significantly improve the removal capacity of selenium. Since the complexation of selenium ions and PAMAM is pH dependent, the adsorbents can be reused after regeneration at high pH solutions.

In this work, graphene oxide was first modified by 3-aminopropyltriethoxysilane (APTES). Different generations of PAMAM were then in-situ grafted onto the surface of modified GO by repetition of a two-step method. The adsorbents are added into the selenium containing solution first. After the adsorption process, PAMAM-GO could be separated from the solution by filtration.

1.5 Outline of Thesis

Background of selenium pollution, poly (amido amine) and graphene/graphene oxide (GO) are introduced in Chapter 1.

Chapter 2 describes the synthesis procedure of GO and dendrimer-functionalized graphene oxide (PAMAM-GO). The characterization methods (principles and application) and selenium adsorption tests are also listed in this chapter.

The characterization results are shown in Chapter 3, including TEM, FTIR, XPS, XRD and TGA analysis.

The effects of dendrimer generation, initial Se concentration and initial pH of solution are discussed in Chapter 4. PAMAM-GO show increasing removal ability with increasing dendrimer generation. GO-G4 has a removal capacity of 60.9 mg g^{-1} in Se (IV) and 77.9 mg g^{-1} in Se (VI) at pH 6. The adsorbent shows higher removal capacity under lower pH, achieving 38.8 mg g^{-1} in Se (IV) and 127 mg g^{-1} in Se (VI) respectively under pH 3.

Chapter 2 Experimental Section

2.1 Chemicals

Natural graphite (7-10 micron), potassium permanganate ($KMnO_4$), sodium nitrate ($NaNO_3$) and H_2O_2 (30 wt.%) were purchased from Alfa Aesar. Methylacrylate (MA), ethylenediamine (EDA), 3-aminopropyltriethoxysilane (APTES, 99%), ethanol, methanol, H_2SO_4 (98%), HCl (1 N) and NaOH (1 N) were purchased from Fisher Scientific Company, Canada. Milli-Q water was used in all processes of aqueous solution preparation and lavation. All chemicals were used without further purification.

2.2 Adsorbents Synthesis

2.2.1 Synthesis of graphene oxide (GO)

GO was prepared by a modified Hummers method illustrated in earlier work.[94] Typically, 2 g graphite and 1.5 g sodium nitrate were first mixed in a three-necked flask. Sulfuric acid (98%, 150 mL) was then added to the mixture with mechanical stirring in an ice-water bath. Afterwards, 9 g potassium permanganate was slowly (normally over about 1 h) added into the mixture. Stirring was maintained for another 2 h in ice-water bath before the mixture was stirred vigorously for 5 days at room temperature. Subsequently, 6 mL of H_2O_2 was added into the mixture to react with the residual $KMnO_4$. 250 mL of a solution mixed with 7.5 mL H_2SO_4, 4.17 mL H_2O_2 and Milli-Q water was then slowly added into the mixture to the obtained bright yellow suspension with mechanical stirring maintained. The sediment was separated by centrifuge and washed with Milli-Q water repeatedly until neutral pH, followed by another 5 days of dialysis to

remove the soluble ions. Dried GO product was obtained in a fluffy golden flocci form after freeze-drying.

2.2.2 Synthesis of amine-functionalized graphene oxide

GO contains hydroxyl, carboxyl and carbonyl groups on their basal planes and edges, which can react with APTES to achieve the amine-functionalization of GO. Briefly, GO (300 mg) was dispersed in 150 mL ethanol by ultrasonication for 30 min at room temperature. Then 2.3 mL APTES was added dropwise into the suspension under N_2 atmosphere. The mixture was then kept at reflux temperature for 24 h with mechanical stirring. Afterwards, the resulting amine-functionalized GO was filtered, washed five times with ethanol and then freeze dried. The resulting product was denoted as GO-G0.

2.2.3 Synthesis of PAMAM-modified graphene oxide

Synthesis of PAMAM dendrimer on the surface of amine-functionalized GO was achieved according to the methods of Pan[95] and Tajabadi[96] with some modification. The procedure was depicted in Figure 2-1. Firstly, 150 mL of 2 mg/mL GO-G0 methanol solution was sonicated for 30 min to obtain finely dispersed mixture. The solution was then vigorously stirred by magnetic stirrer under N_2 atmosphere. 70 mL of MA solution in methanol (20%, v/v) was then added dropwise to the mixture at 0 °C. Afterwards the flask was sealed and the mixture was stirred at 50 °C for 24 h under N_2 atmosphere. The resulting material (denoted as GO-G0.5) was collected by centrifugation and washed five times with ethanol before freeze drying. Secondly, 100 mL of EDA solution in methanol (50%, v/v) was added into 150 mL GO-G0.5 methanol solution under N_2 atmosphere. The flask was then sealed and vigorously stirred at 50 °C for 24 h. The product (denoted as GO-G1) was washed with ethanol five times and freeze

dried for further use. These two steps were repeated until specified generation of dendrimer obtained. The following generations of PAMAM-GO were denoted as GO-G2, GO-G3 and GO-G4, respectively.

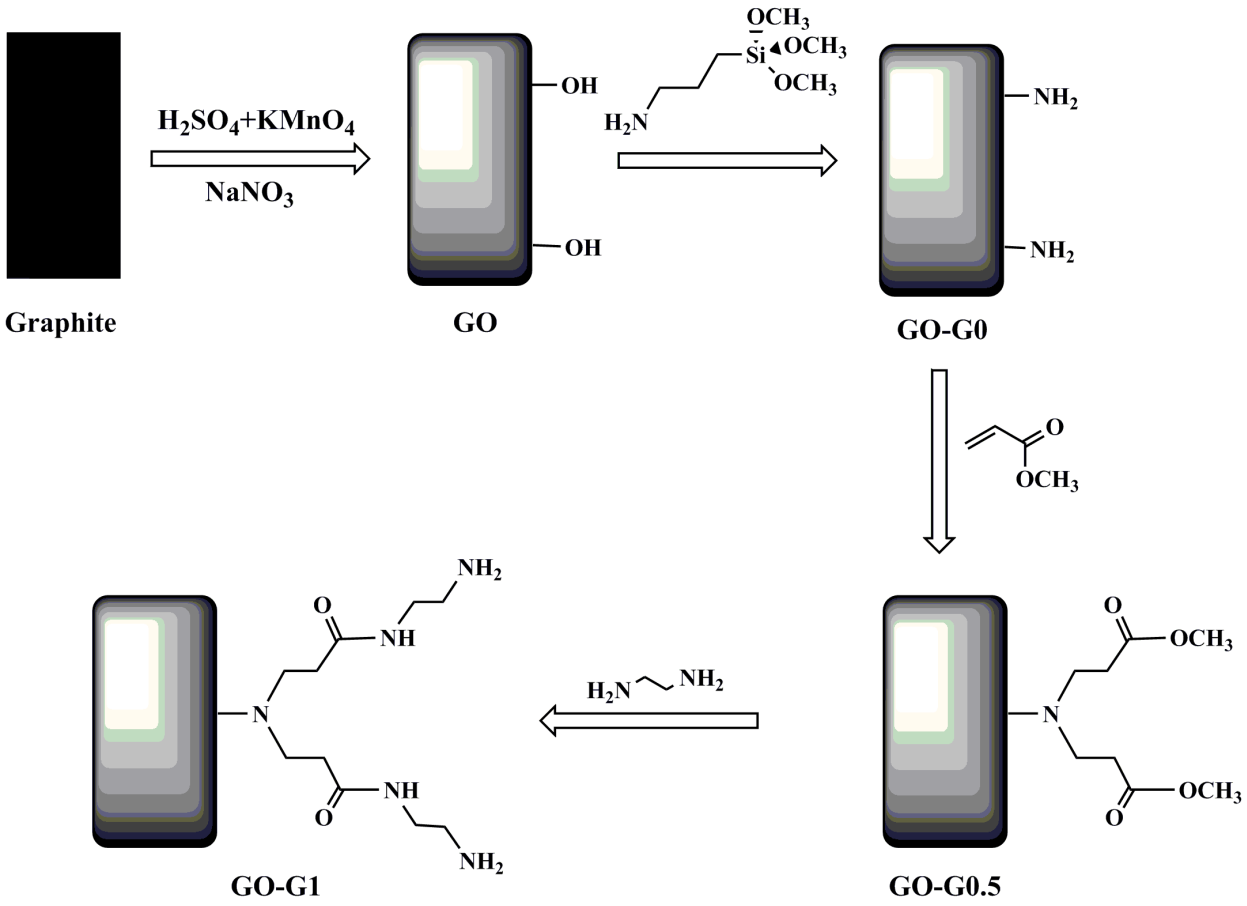

Figure 2-1 Schematic illustration of the synthesis of PAMAM-modified graphene oxide.

2.2 Adsorption Experiments

Different generations of the adsorbent (2 mg, dosage 0.2 g L^{-1}) were added into 10 mL of Se (IV) or Se (VI) solution, and mixed uniformly by shaking at 300 rpm at room temperature (25 °C) for 24 h. NaOH and HCl were applied to adjust the pH of the solutions. The adsorbent was separated by filtration after the adsorption process. The supernatant of Se (IV) and Se (VI) was collected for Inductively Coupled Plasma Mass Spectrometry (ICP-MS) analysis to determine the concentration of selenium ions. The adsorption amount q (mg g^{-1}) is defined in the following equation, where C_0 (ppm) is the initial Se (IV) or Se (VI) concentration, C_e (ppm) is the equilibrium concentration of Se (IV) or Se (VI), W (mg) is the adsorbent weight, V (mL) is the total solution volume.

$$q = \frac{(C_0 - C_e) \times V}{W} \tag{2-1}$$

2.3 Characterization Methods

2.3.1 TEM

The Transmission Electron Microscopy (TEM) has become the premier tool for the microstructural characterization of materials.[97] It utilizes energetic electrons to provide high-resolution morphologic, compositional and crystallographic information on samples.[98]

In a conventional TEM, a thin specimen is irradiated with an electron beam of uniform current density. Electrons are emitted in the electron gun by thermionic, Schottky, or field emission. The latter are used when high gun brightness and coherence are needed. The electrons then pass through multiple electromagnetic lenses to the screen, where the electrons are

converted to light to form an image. In the images, the lighter areas represent the places where more electrons pass through, while the darker areas reflect the dense areas of the object. These differences provide information on the structure, texture, shape and size of the sample.[99-100]

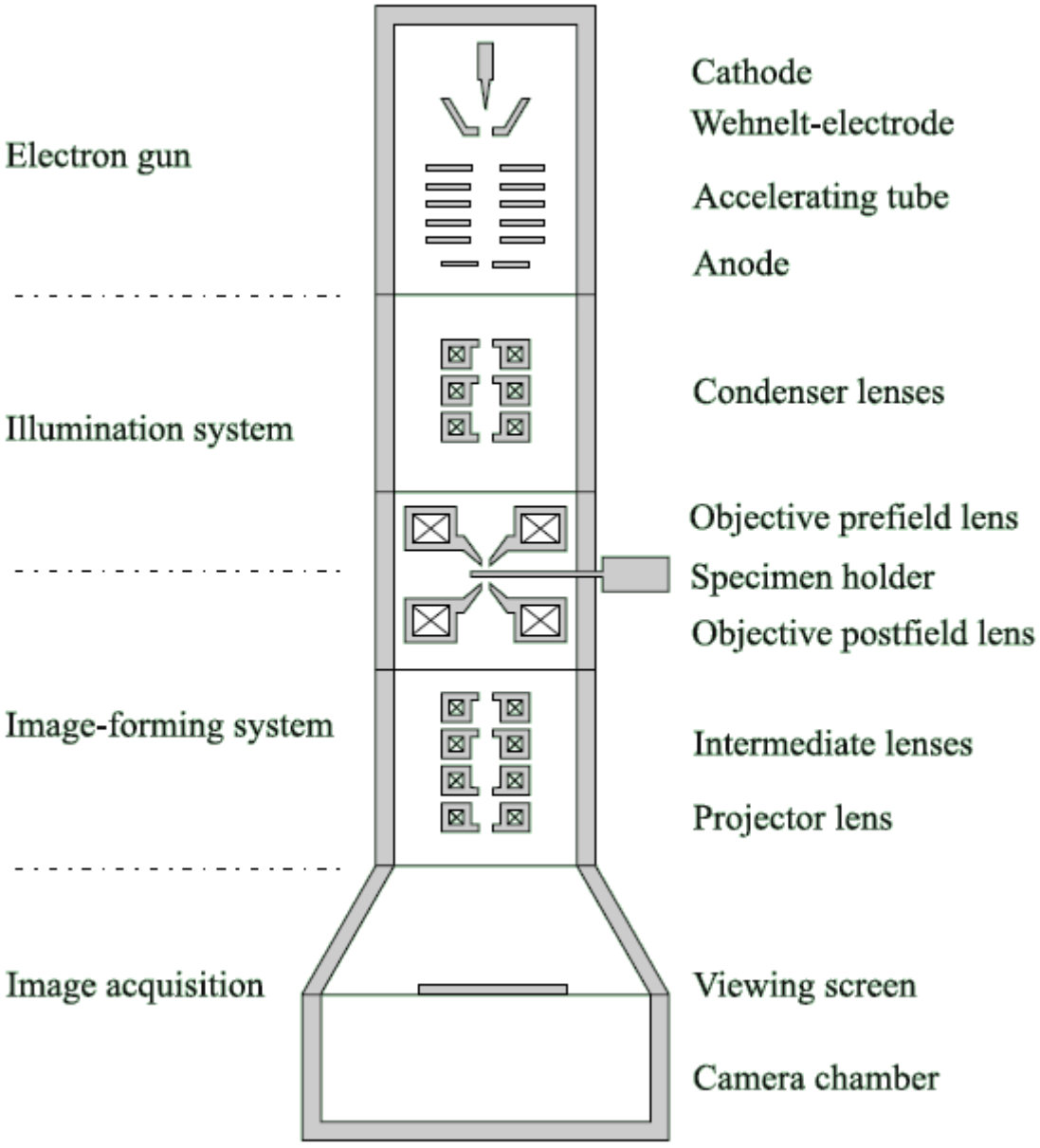

Figure 2-2 Basic components of a TEM.[101]

In this work, TEM is mainly applied to observe the morphology of GO and PAMAM-GO. The characterization of the morphology was performed by TEM using a Hitachi HF 3300 Mode. TEM samples were prepared by pipetting several microliters of GO and PAMAM-GO dispersion onto lacey carbon coated copper grids and dried.

2.3.2 Fourier Transform Infrared Spectroscopy (FTIR) analysis

Fourier transform infrared (FTIR) spectroscopic imaging is a relatively new method that has received great attention as a new field of analytical chemistry.[102] It is widely used in characterization of various fields, ranging from molecular complexes to cells or tissues. Infrared radiation is divided into three regions: near-infrared region (10,000 - 4,000 cm^{-1}), mid-infrared region (4,000 - 200 cm^{-1}), and far-infrared region (200 - 10 cm^{-1}).[103]

Infrared spectroscopy (IR) probes the molecular vibrations. A normal mode of vibration is infrared active (i.e., it absorbs the incident infrared light) if there is a change in the dipole moment of the molecule during the course of the vibration. The asymmetric vibrations of all molecules can be detected by IR. The vibrational frequencies of a given chemical group are expected in specific regions which depend on the type of atoms involved and the type of chemical bonds.[104]

Dispersive IR spectrometers are slowly being replaced by quicker and more sensitive Fourier transform (FT) instruments. The greater sensitivity of the FTIR spectrometers is related to the continuous detection of the entire transmitted energy simultaneously, using interferometers, and rapid Fourier transformation of the interferogram into a spectrum. The increased sensitivity of FTIR spectrometers led to the development and recent broad application of reflectance techniques, such as ATR and DRIFT.[105]

The FTIR spectrometer has several advantages including: (1) higher signal-to-noise ratio (SNR); (2) high accuracy of wavenumber, with the error range within ± 0.01 cm^{-1}; (3) rapid scanning (1 s or less); and (4) extremely high resolution (0.1 ~ 0.005 cm^{-1}).[106]

Typical setup of a Fourier transform infrared (FTIR) spectrometer is shown in Figure 2-3: the light from an infrared light source is sent through an aperture hole to the beam splitter that sends two equivalent beams (one reflected and one transmitted) to a fixed and to a scanning mirror, respectively. After acquiring different optical path lengths (in addition to the equal distances of both mirrors from the beamsplitter – the 'zero path difference') these two beams recombine on the beamsplitter and are sent to the sample, then to a semiconductor detector. The detector signal as function of the optical path difference between the two mirrors is the interferogram. After calculation the infrared spectrum is obtained.[107]

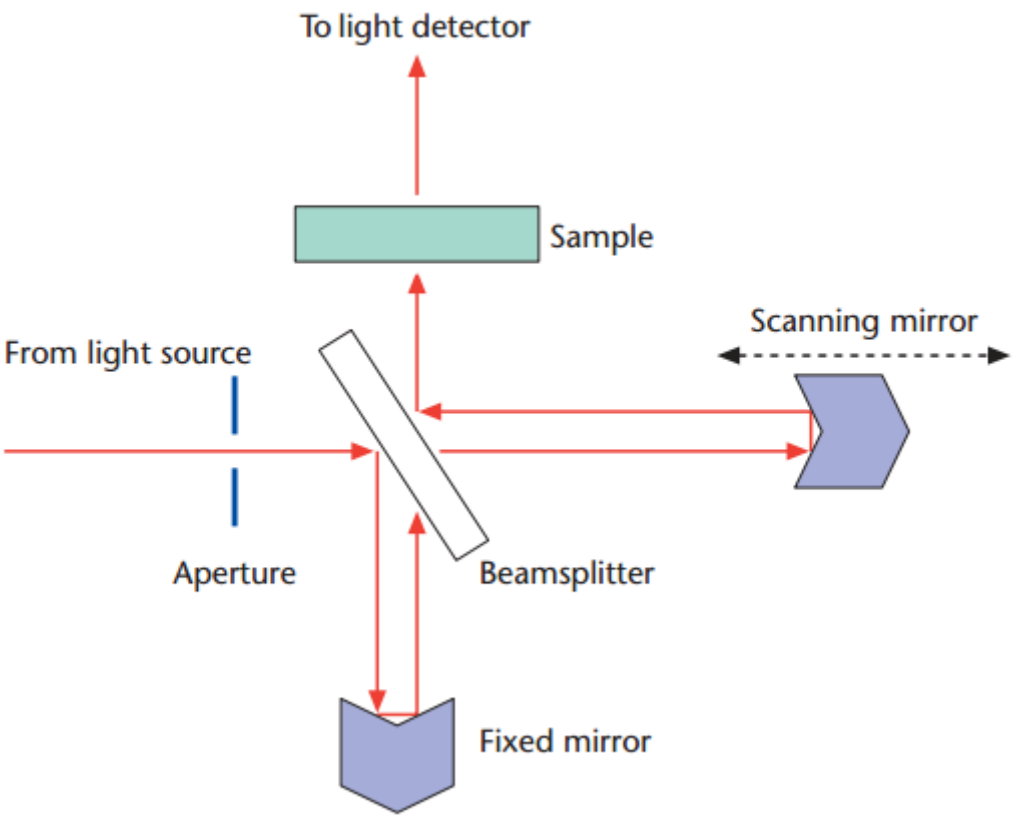

Figure 2-3 A schematic representation of an interferometer used in FTIR spectrometers.[107]

In this project, FTIR spectra were recorded on Nicolet iS50 FT-IR Imaging System, and is mainly applied for the determination of the functional groups on GO and differenent generations of PAMAM-GO.

2.3.3 XPS analysis

X-ray photoelectron spectroscopy (XPS) is generally regarded as an important and key technique for the surface characterization.[108] It provides a total elemental analysis, except for hydrogen and helium, of the top 10-200 Å (depending on the sample and instrumental conditions) of any solid surface which is vacuum stable or can be made vacuum stable by cooling. The information content in a typical XPS spectrum is enormous, including: (1) simple elemental

analysis; (2) detailed considerations of chemical shifts and chemical bongding nature in the surface region; and (3) various loss or relaxation structures which provide further information on the chemical nature of the surface.[109]

Surface analysis by XPS is accomplished by irradiating a sample with monoenergetic soft x-rays, causing electrons to be emitted and analyzing the energy of the detected electrons. The emitted electrons have kinetic energies given by:[110]

$$KE = h\nu - BE - \varphi_s \tag{2-2}$$

where $h\upsilon$ is the energy of the photon, BE is the binding energy of the atomic orbital from which the electron originates, and φ_s is the spectrometer work function.

Each element has a unique set of binding energies, XPS can be used to identify and determine the concentration of the elements in the surface. Variations in the elemental binding energies arise from differences in the chemical potential and polarizability of compounds, which can be used to identify the chemical state of the materials being analyzed.[110]

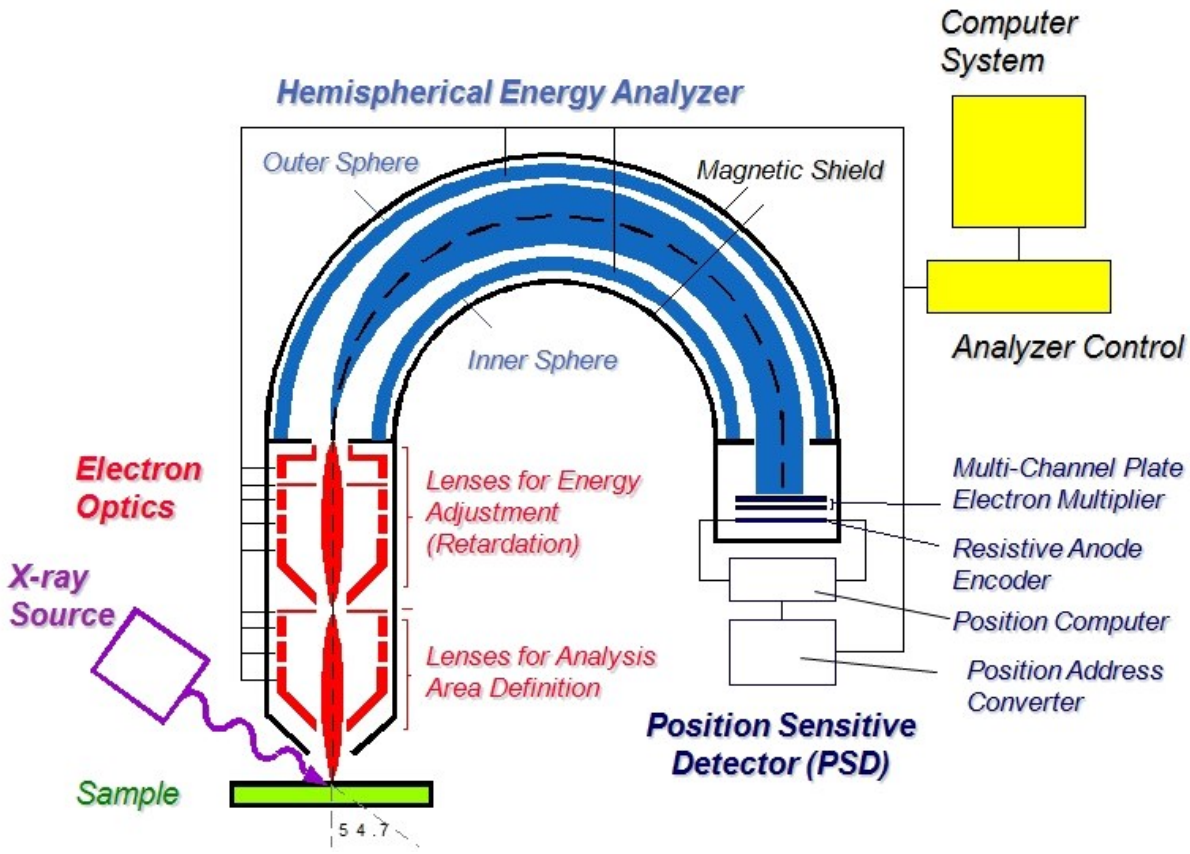

Figure 2-4 Basic mechanism of XPS.[111]

In this thesis, XPS analysis was conducted using AXIS 165 XPS Spectrometer. All the bonding energies have been corrected by referring to the C 1s photoelectron peak at 284.6 eV. In this work, XPS was used to determine the chemical bonds between PAMAM and graphene oxide.

2.3.4 XRD

A crystal is a periodic array of atoms or molecules, where each element of the smallest repeating unit makes the same kind of interaction with its neighbors. The smallest repeating unit of a crystal is termed the asymmetric unit. Diffraction is observed when waves are scattered by a periodic array that is arranged with the appropriate spacing to fulfill Bragg's law:[112]

$$2d \sin\theta = \mathrm{n}\lambda \tag{2-3}$$

Bragg's law is satisfied when a lattice with a characteristic spacing (d) scatters incident radiation of an integral (n) number of wavelengths (λ), which interfere with each other constructively and destructively to give rise to a diffracted wave. A diffracted wave is observed at a characteristic scattering angle (θ) relative to the source.[112]

Figure 2-5 shows the schematic illustration of X-ray diffractometer. O is an axis perpendicular to the plane. The X-ray source is S, the line focal spot on the target T of the X-ray tube. X-rays diverge from S and are diffracted by the specimen C to form a convergent diffracted beam which comes to a focus at the slit F and then enters the counter G.[113]

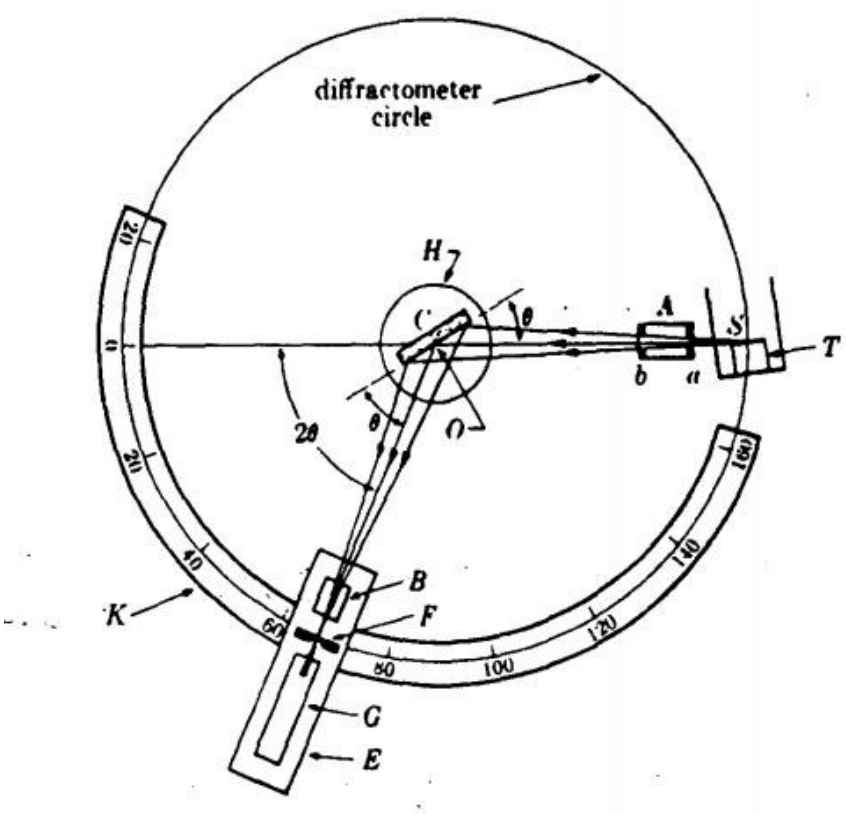

Figure 2-5 Schematic illustration of X-ray diffractometer.[113]

In this work, X-ray Diffraction analysis was taken on a RIGAKU Rotating anode XRD system with a copper anode, 40 kV, 2 degs minute^{-1}. XRD analysis would identify the substance of GO, PAMAM-GO and iron oxide.

2.3.5 TGA analysis

In thermogravimetric analysis (TGA), changes in weight are measured as a function of increasing temperature or time under a precisely controlled atmosphere.[114] TGA can provide information about physical phenomena, such as second-order phase transitions, including vaporization, sublimation, absorption, adsorption, and desorption. Likewise, TGA can provide information about chemical phenomena including chemisorptions, desolvation (especially dehydration), decomposition, and solid-gas reactions (e.g., oxidation or reduction).[114]

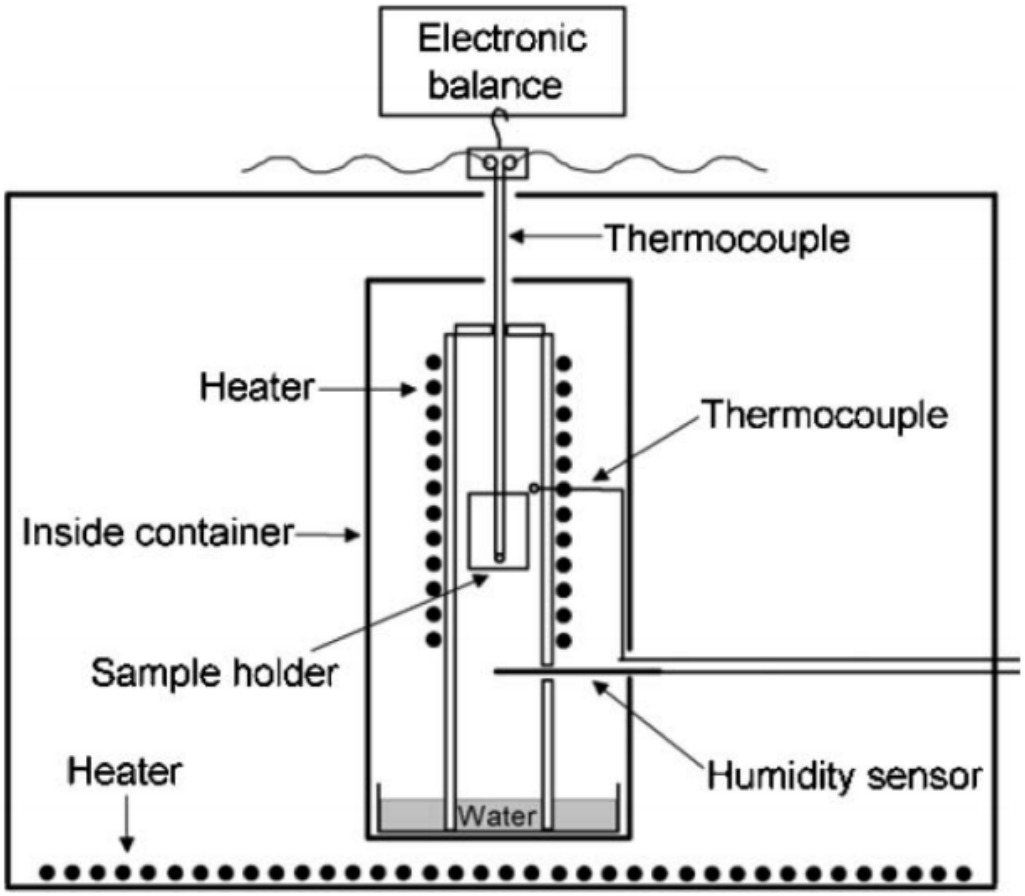

Figure 2-6 Schematic diagram of TGA instrument.[115]

In this thesis, TGA was conducted with TA Instrument Q-500 equipment, using nitrogen as the purge gas. The heating rate was 1 °C min^{-1}. Before the tests, all the samples were carefully ground to powders to ensure sufficient diffusion of heat.

2.3.6 Zeta potential measurement

Relative motion between the particle surface and the electrolyte, for example, due to fluid flow, results in shear within the electrical diffuse layer under applied voltage. The plane along which such shearing occurs is called the "slipping plane," and the electrical potential along this

plane is defined as the zeta potential (shown in Figure 2-7).[116] In other words, zeta potential is the potential difference between the dispersion medium and the stationary layer of fluid attached to the dispersed particle.[117]

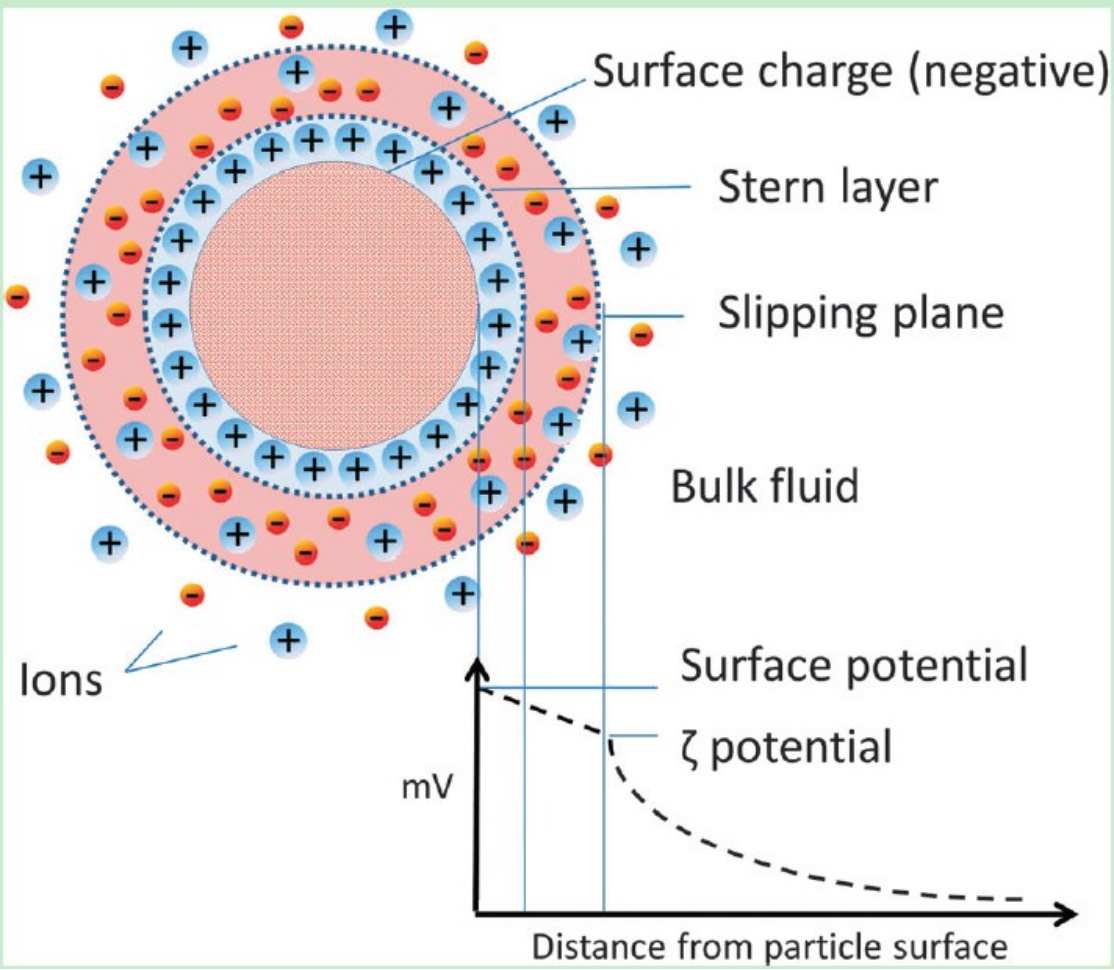

Figure 2-7 Schematic representation of zeta potential.[118]

Zeta potential can be used to determine surface isoelectric points and quantify a change in surface ionizable groups.[119] It is a key indicator of the stability of colloidal dispersions. For molecules and particles that are small enough, a high zeta potential will confer stability, i.e., the

solution or dispersion will resist aggregation. When the potential is small, attractive forces may exceed this repulsion and the dispersion may break and flocculate.[120-121]

In this thesis, zeta potential measurements were performed on Nanosizer Nano (Marlven). All samples were dispersed in 1 mM NaCl aqueous solution by ultrasonication. Zeta potential for PAMAM-GO was used to determine the surface charge properties and stability in water.

2.3.7 ICP-MS

Inductively coupled plasma-mass spectrometry (ICP-MS) is accepted as the most powerful multi-element analytical technique available today, capable of true multi-elemental determinations within minutes. It has become one of the most important techniques for the determination of over 70% of the elements of the periodic table.[122]

The sample, typically introduced into the ICP-MS in a liquid form, is pumped into the sample introduction system, which is made up of a spray chamber and a nebulizer. It emerges as an aerosol that is introduced through the injection channel of the ICP torch into the base of the plasma. The plasma (a highly ionized gas) contains different heating zones where the sample is successively dried, vaporized, atomized, and ionized. During this time, the sample is transformed from a liquid aerosol to solid particles, then into a gas. The so-called analytical zone of the plasma, at approximately 6000 – 7000 K, contains the highest population of excited atoms and monoatomic positively charged ions, representing the elemental composition of the sample. The highly efficient ion extraction, ion transportation through the mass spectrometer and detection is what gives to ICP-MS its ultratrace elemental detection features.[123] Additionally, ICP-MS provides selective multi-elemental (and multi-isotope) detection capabilities to simultaneous

monitoring of the different mass to charge (*m/z*) ratios of the different isotopes. Such information can be used for confirmation purposes and allows, also, the quantification of such elements by applying isotope dilution strategies.[124]

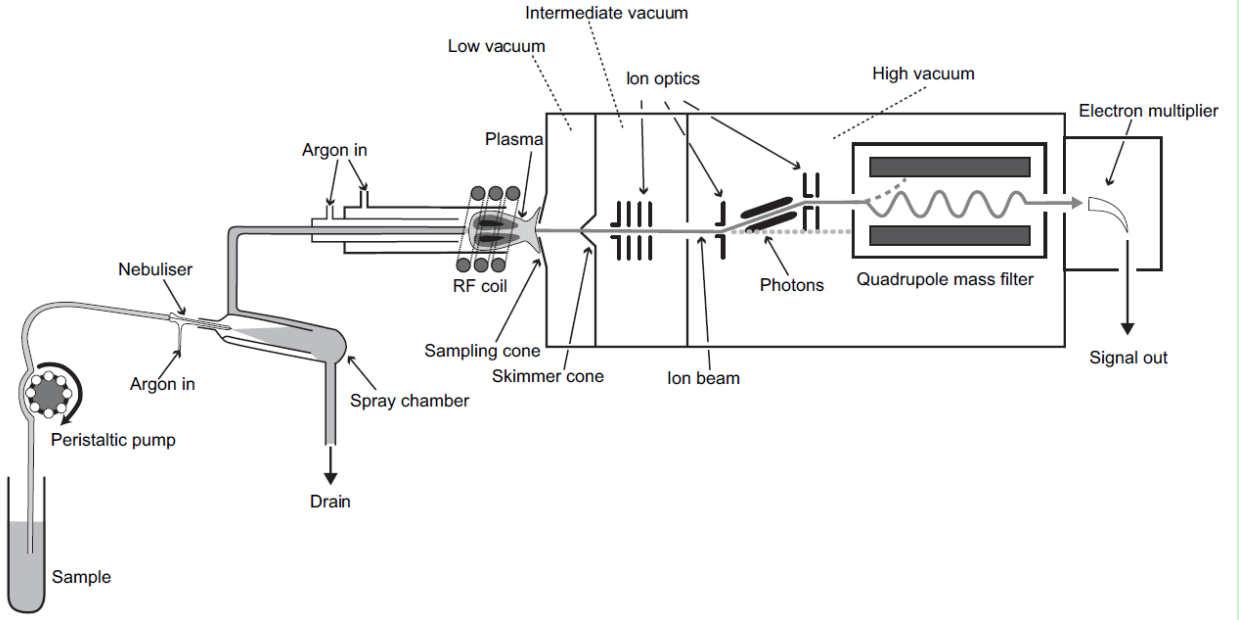

Figure 2-8 Schematic diagram of the major components of an ICP-MS instrument.[122]

Perkin Elmer's Elan 6000 Inductively Coupled Plasma-Mass Spectrometry (ICP-MS) was used to detect the concentration of selenium before and after the adsorption process.

Chapter 3 Characterization

3.1 TEM imaging

Figure 3-1 shows the TEM images of graphene oxide and GO-G4. Compared to the relatively smooth surface of graphene oxide (Figure 3-1a), new species (corresponding to PAMAM molecules) with high density could be observed on the surface of GO-G4 (Figure 3-1b), indicating successful functionalization of PAMAM on graphene oxide surface.[125] The covalent bonding can be further proved by FTIR spectroscopy.

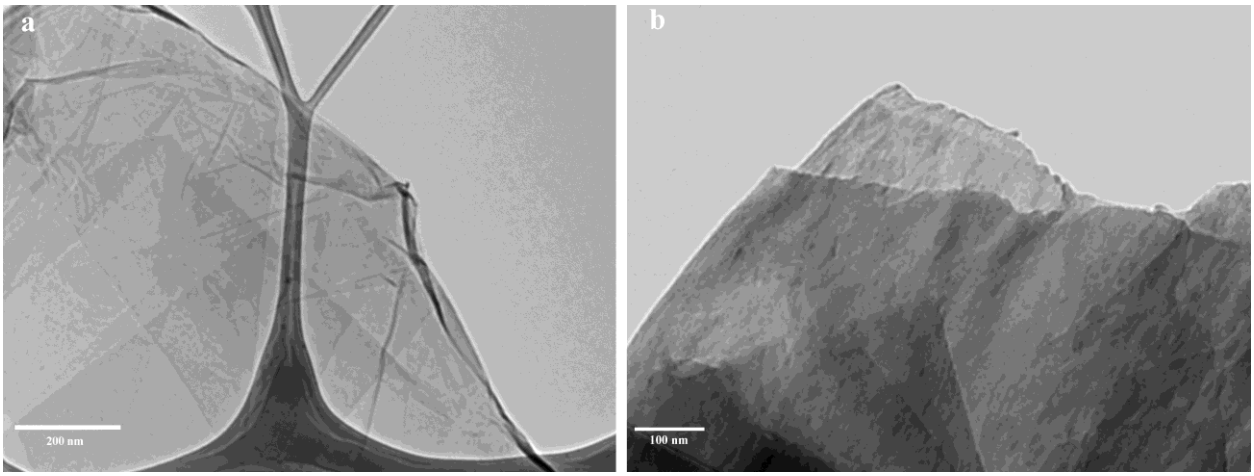

Figure 3-1 TEM images of graphene oxide (a) and GO-G4 (b).

3.2 Fourier Transform Infrared Spectroscopy (FTIR) analysis

The Fourier Transform Infrared Spectroscopy (FTIR) spectra of GO and different generations of PAMAM-GO are shown in Figure 3, indicating the dendrimer modification process. In the FTIR spectra of GO, the peaks observed at 1620 $cm^{-1}$and 1730 cm^{-1} are attributed to the presence of C=C and C=O, respectively. A broad peak at around 3200 cm^{-1} is also observed due to the presence of hydroxyl groups on the basal plane of GO. However, after the

modification with APTES and different generations of PAMAM, this peak significantly decreases, indicating a loss of hydroxyl groups, caused by the reaction between hydroxyl group and silane group. After the silanization of GO by APTES, a peak at around 1550 cm^{-1} can be observed, indicating the successful functionalization of GO by APTES and the existence of amine groups. It can also be proved by the peaks observed at 2873 cm^{-1}, 2938 cm^{-1} and 2971 cm^{-1}, which are attributed to the asymmetric or symmetric stretch of C-H bond in methyl or methylene groups.[38, 126] As the generation increases, the intensity of the band of amine groups increases significantly compared to that of C=C band.

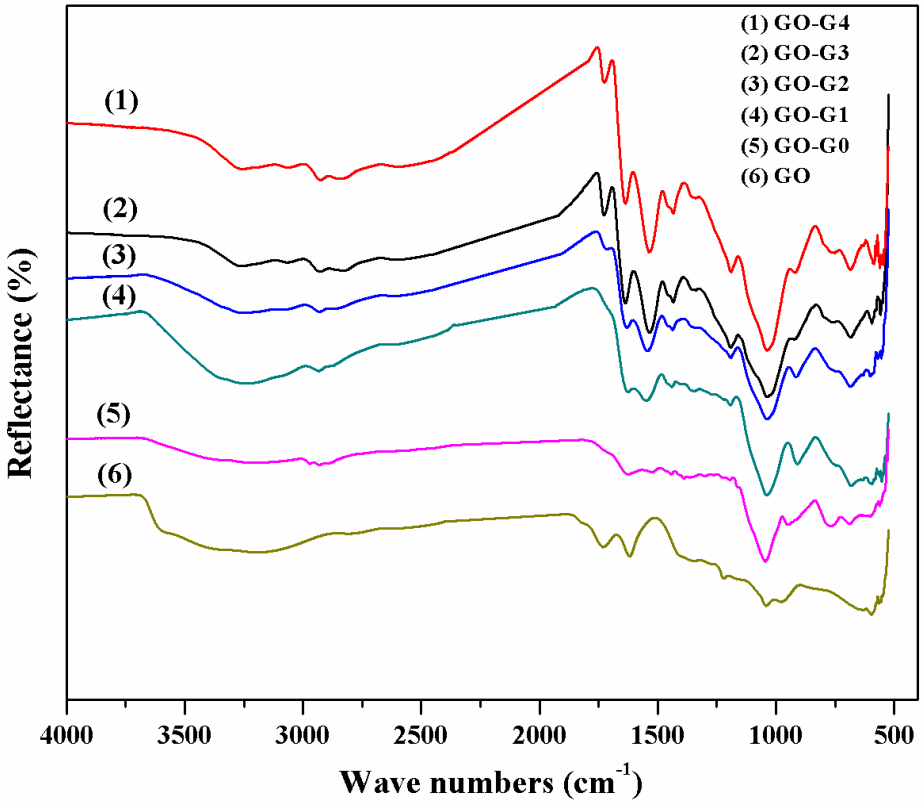

Figure 3-2 FTIR spectra of GO and PAMAM-GO with different generations.

3.3 X-ray Photoelectron Spectroscopy (XPS) analysis

The X-ray Photoelectron Spectroscopy (XPS) spectra of GO and different generations of PAMAM-GO are shown in Figure 3-3. As shown in Figure 3-3a, the XPS spectra of GO mainly shows the C 1s and O 1s peaks, while different generations of PAMAM-GO exhibit a N 1s peak in XPS spectra, indicating the modification process, which is consistent with the FTIR results. The ratio of N/Si was found to increase with the generation, showing the propagation of dendrimers. The XPS analysis of C 1s spectra (Figure 3-3b and 3-3c) show detailed functional groups on the surface of different kinds of materials. It is shown in Figure 3-3b that there are three main types of carbon species in graphene oxide, C-C at 284.6 eV， C-O at 286.7 eV and C=O at 288.2 eV. Compared to graphene oxide, the C 1s XPS spectra of GO-G4 shows a significant decrease at 286.7 eV. This indicates the loss of C-O which may be caused by the reaction between hydroxyl groups and silane groups. Moreover, there are two new peaks observed at 285.4 eV and 286.1 eV corresponding to the existence of C-NH_2 and C-N bonds respectively.[127] The successful introduction of primary amine groups can also be proved by the N 1s XPS spectra of GO-G4, the peaks appear at 399.9 eV and 401.1 eV are attributed to amines NH_2 and amide bonds N-C=O respectively.[128-129]

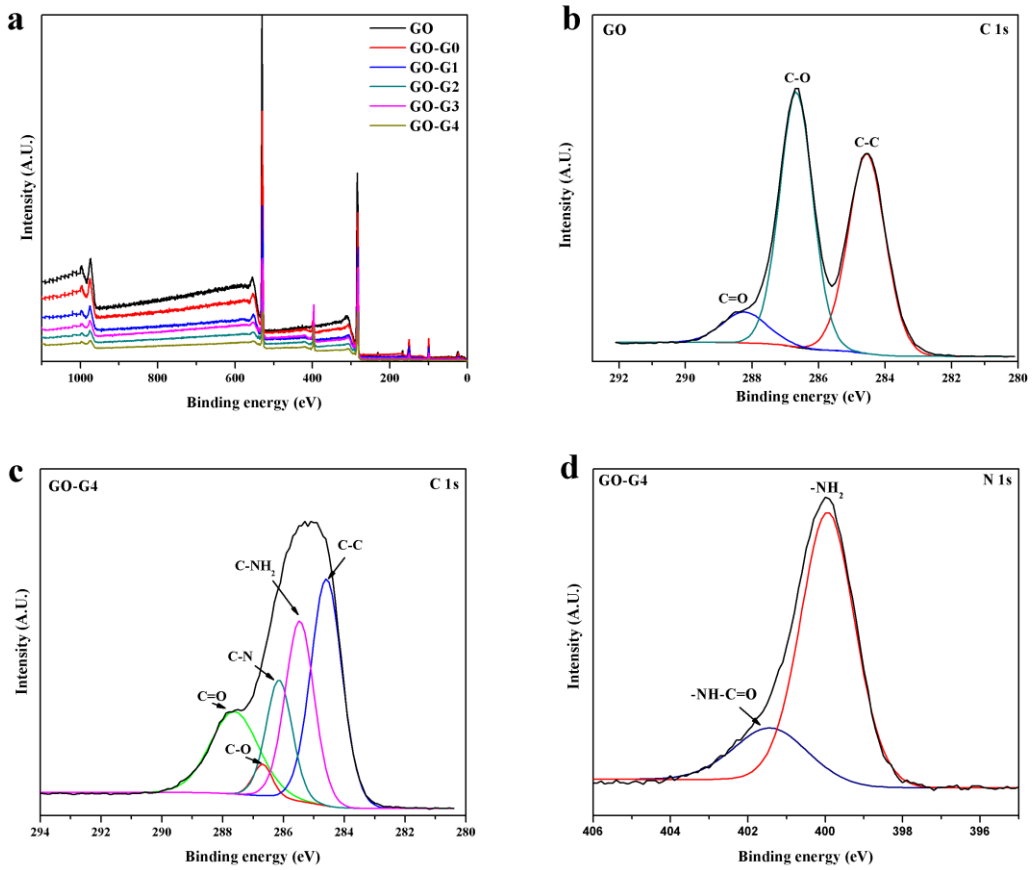

Figure 3-3 (a) XPS of GO and PAMAM-GO with different generations; (b) the C1s XPS spectra of GO; (c) the C1s XPS spectra of GO-G4; (d) the N1s XPS spectra of GO-G4.

3.4 X-ray Diffraction (XRD) analysis

The X-ray diffraction (XRD) patterns of GO, GO-G0 and GO-G3 are shown in Figure 3-4. According to Bragg Equation ($2d\sin\theta=\lambda$, λ is the wavelength of X-ray, ~ 1.54 Å), the interlayer space of GO is 7.7 Å at $2\theta=11.4°$. The XRD pattern of GO-G4 shows a broad peak at $2\theta=15\text{-}35°$, which indicates that the PAMAM-modified graphene oxide exist in a form of noncrystalline state.[130]

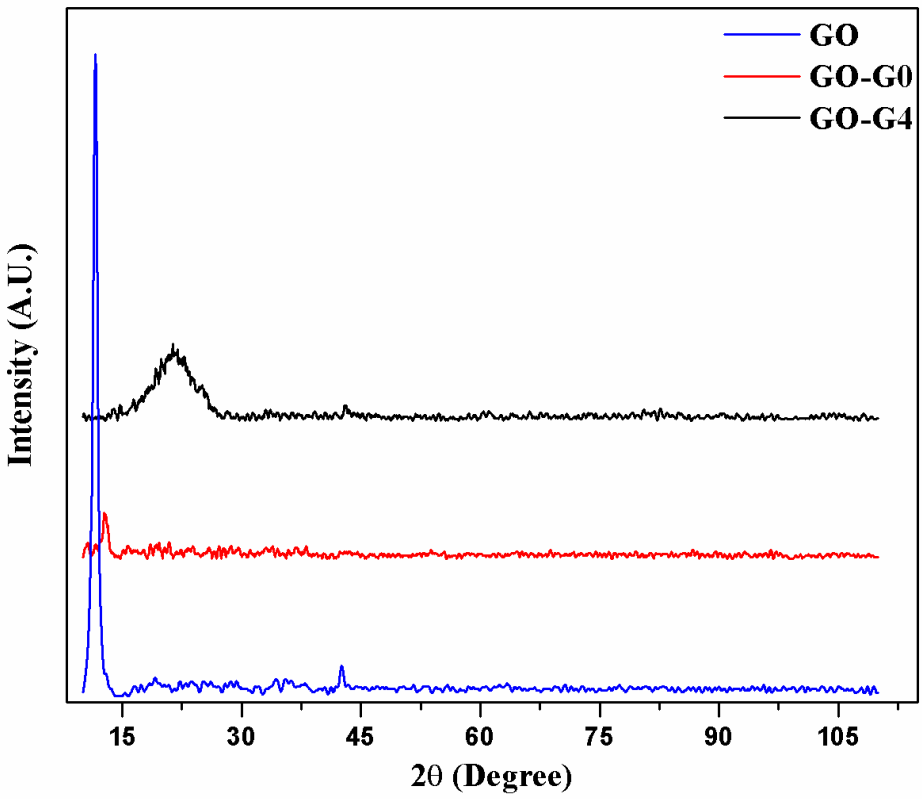

Figure 3-4 X-ray diffraction patterns of GO, GO-G0 and GO-G4.

3.5 Thermal Gravimetric Analysis (TGA) analysis

The TGA curves of GO and PAMAM-GO are shown in Figure 3-5. For GO, the weight loss started from ~ 20 °C to ~ 120 °C could be attributed to adsorbed water. The most significant weight loss occurs at around 160 °C, which may be due to pyrolysis of the labile oxygen-containing functional groups, yielding CO, CO_2, and steam.[131-132] The further mass loss starting at around 600 °C is attributed to the pyrolysis of the carbon skeleton of GO.[133] Compared with the curve of GO, GO-G0 shows less weight loss below 200 °C, indicating much of hydroxyl and epoxy groups have been converted after the silanization reaction with APTES. A weight loss

between 500 °C and 600 °C is caused by the pyrolysis of silane moieties of GO-G0.[133] As shown in Figure 3-5b, the TGA curves of different generations of PAMAM-GO presents a weight loss of 8.5 %, 12.89 %, 15.84 % and 19.4 % (generations 1-4, respectively), occurring between 280 °C and 450 °C.[134-135]

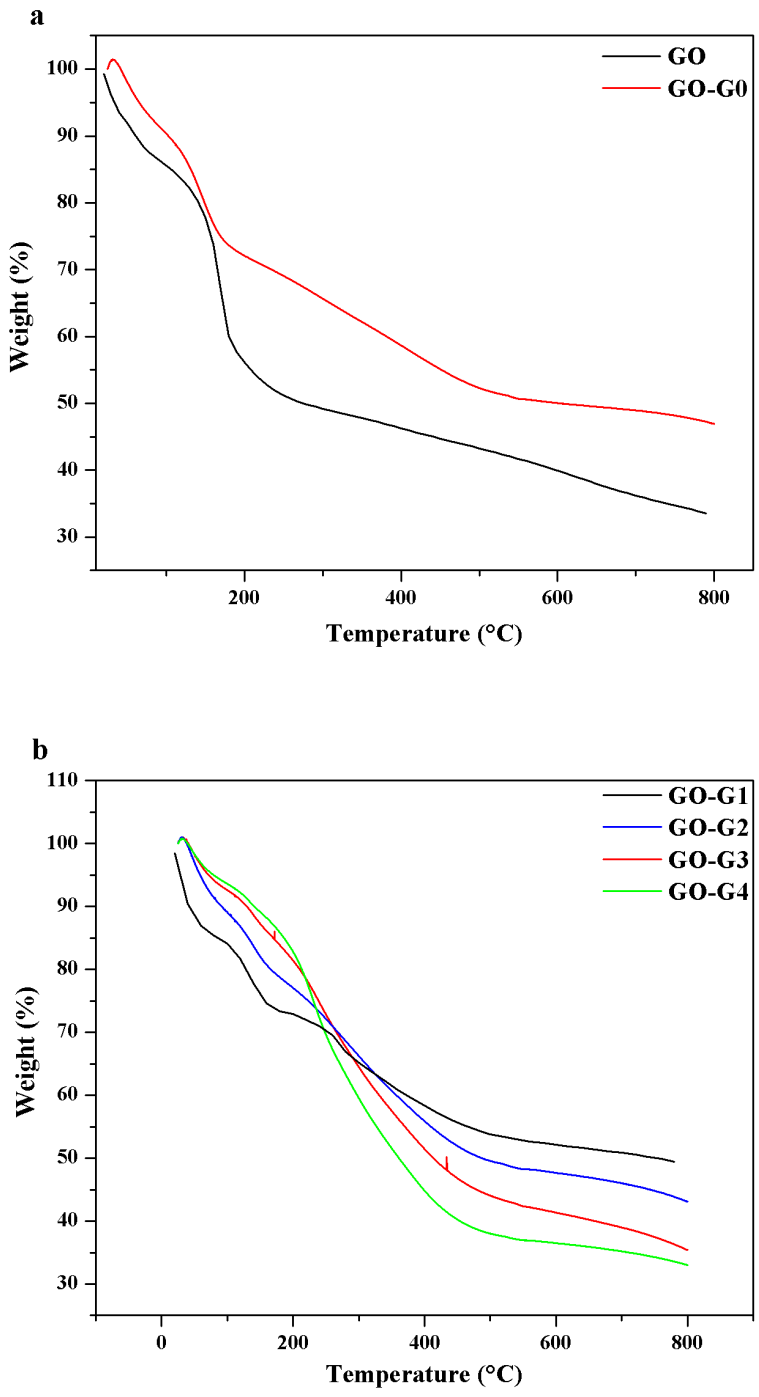

Figure 3-5 TGA curves of (a) GO, GO-G0 and (b) different generations of PAMAM-GO.

Chapter 4 Adsorption Tests

4.1 Effect of generation on selenium removal capacity

Different generations (0-4) of the adsorbents were applied for the removal of selenium oxyanions. As shown in Figure 4-1, the adsorption amount of Se (VI) shows a significant increase from GO-G0 to GO-G4, which is attributed to the increase of amine groups. However, the adsorption amount of Se (IV) on PAMAM-GO exhibits differently. It reaches the highest value when GO-G3 is applied as the adsorbent, and then drops when the generation continues increasing. The results will be discussed later in the mechanism session.

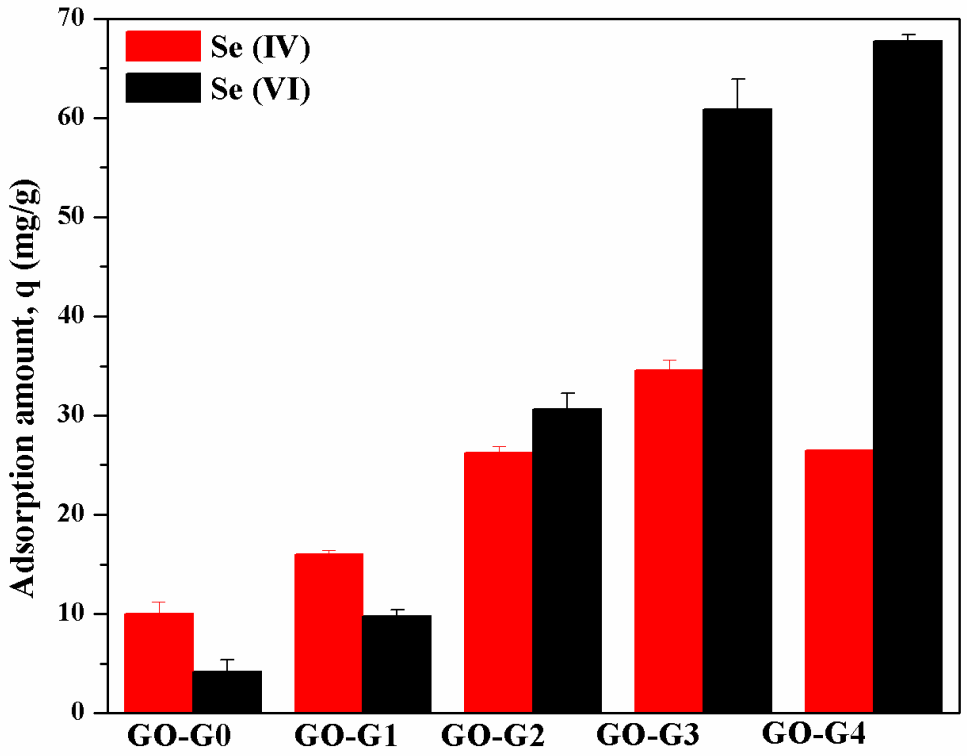

Figure 4-1 Comparison between different generations of PAMAM-GO for adsorption of Se (IV) and Se (VI) ions at C_0 = 40 ppm, pH = 6.

4.2 Comparison between GO-G4 and MGO for selenium adsorption

The comparison between GO-G4 and MGO (synthesized by co-precipitation method[87]) for both Se (IV) and Se (VI) ions adsorption at different concentrations are shown in Figure 4-2a and Figure 4-2b. GO-G4 exhibits stronger adsorption capability than MGO in both Se (IV) and Se (VI) ions removal. For selenite ions removal, GO-G4 shows higher adsorption amount obviously under higher concentration, while it does not show significant increase compared to MGO under lower concentration. However, for the selenate ions, GO-G4 shows much stronger

adsorption capability from ~20 ppb to ~80 ppm, indicating PAMAM-GO has higher selectivity in Se (VI) removal. The difference can be attributed to the different mechanisms for each kind of selenium oxyanion. The mechanisms will be discussed later.

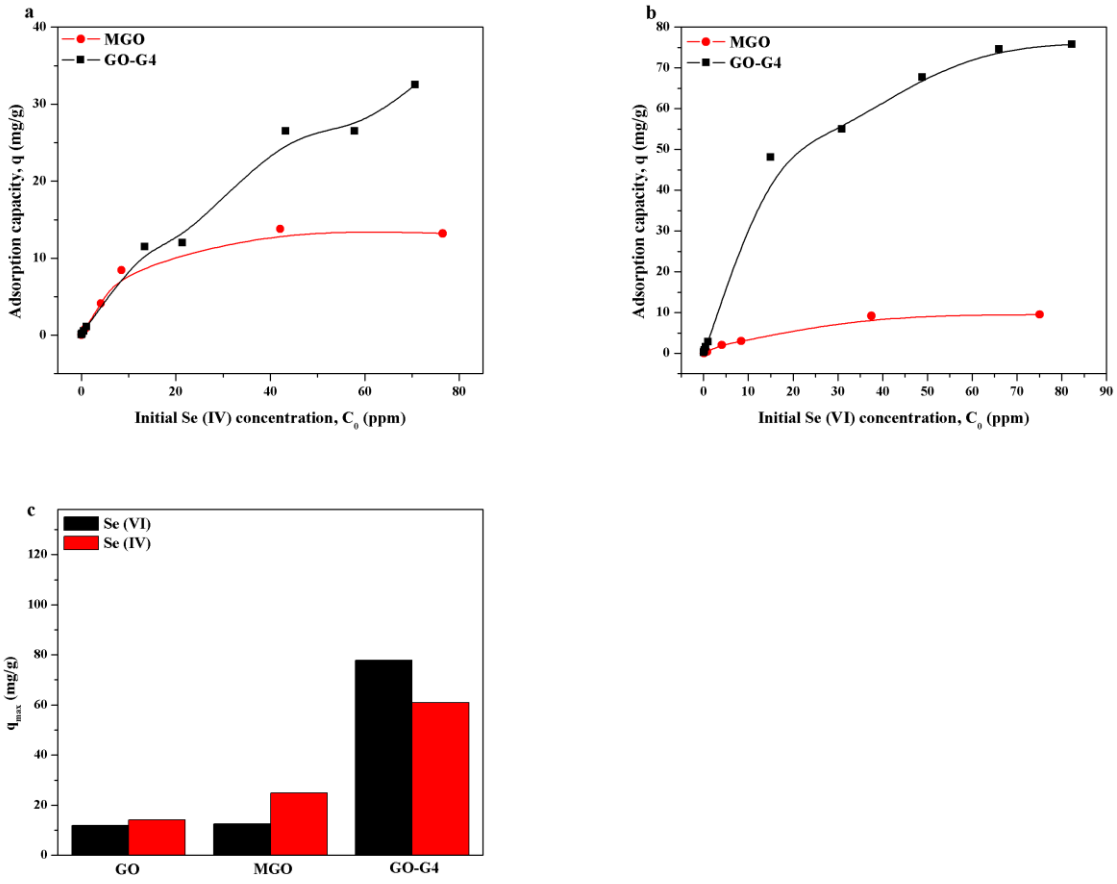

Figure 4-2 (a), (b): Comparison between GO-G4 and MGO for adsorption of Se (IV) and Se (VI) ions at different initial selenium concentrations (pH = 6). (c) Comparison of maximum adsorption capacity between GO-G4, GO and MGO (MGO data obtained from previous work[136]).

4.3 Effect of initial selenium concentration on adsorption isotherms - Langmuir and Freundlich adsorption models

The commonly used Langmuir and Freundlich adsorption models were applied for study the isotherms of Se (IV) and Se (VI) ions removal on GO-G4. The Langmuir isotherm is expressed as follows:[90]

$$q = \frac{q_{\max} b C_e}{1 + b C_e} \tag{4-1}$$

where q_{max} (mg g^{-1}) is the maximum amount of adsorption; b (L mg^{-1}) is the Langmuir adsorption equilibrium constant, C_e (mg L^{-1}) is the equilibrium concentration of pollutant in the liquid phase.

The Freundlich equation is represented as follows:[89]

$$q = K_F C_e^{\,n} \tag{4-2}$$

where K_F and n are Freundlich constants. K_F represents adsorption capacity and n represents the degree of dependence of adsorption at the equilibrium concentration. When n is between 0.1 and 1, the adsorption process is considered as optimal adsorption; while when $n > 2$, the adsorption is difficult to occur.[87, 137-138]

The isotherm parameters and correlation coefficients are shown in Table 4-1. The n values in Freundlich equation are less than 1 for both Se (IV) and Se (VI) removal, indicating the adsorption processes of Se (IV) and Se (VI) were favorable. The results show the Langmuir equation provides a better fitting for both Se (IV) and Se (VI) adsorption with higher R^2 values,

which means GO-G4 provided homogeneous adsorption sites in the process of selenium removal. The maximum removal capacity obtained from Langmuir equation for Se (IV) and Se (VI) are 60.9 mg g^{-1} and 77.9 mg g^{-1}, respectively. The maximum capacity of GO-G4 shows a significant increase compared to GO and MGO, shown in Figure 4-2c.

Table 4-1 Parameters of Langmuir and Freundlich models for adsorption of Se (IV) and Se (VI) ions on GO-G4.

Isotherm type	Isotherm constants	Se (IV)	Se (VI)
Langmuir	q_{max} [mg g^{-1}]	60.893	77.856
	b [L mg^{-1}]	0.0170	0.2220
	R_L^2	0.982	0.985
Freundlich	K_F	2.048	17.472
	n	0.664	0.369
	R_F^2	0.980	0.945

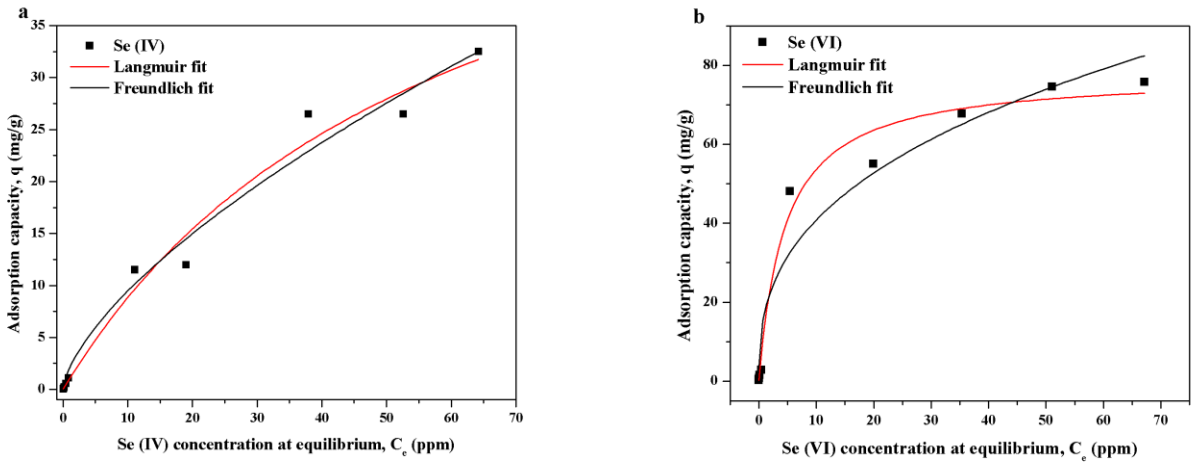

Figure 4-3 Fitting curves using Langmuir and Freundlich models under different (a) Se (IV) and (b) Se (VI) equilibrium concentrations.

4.4 Effect of initial pH on selenium adsorption

As shown in Figure 4-4, the removal capacity of Se (VI) increased dramatically with pH decreased, and reached a capacity of 127 mg g^{-1} at pH = 3. By contrast, the removal capacity of Se (IV) also gradually increased with decreasing pH, but did not show significant change. The phenomenon show that lower pH will facilitate the adsorption of both Se (IV) and Se (VI) ions on GO-G4, but the initial pH influences the adsorption of Se (VI) much more than that of Se (IV).

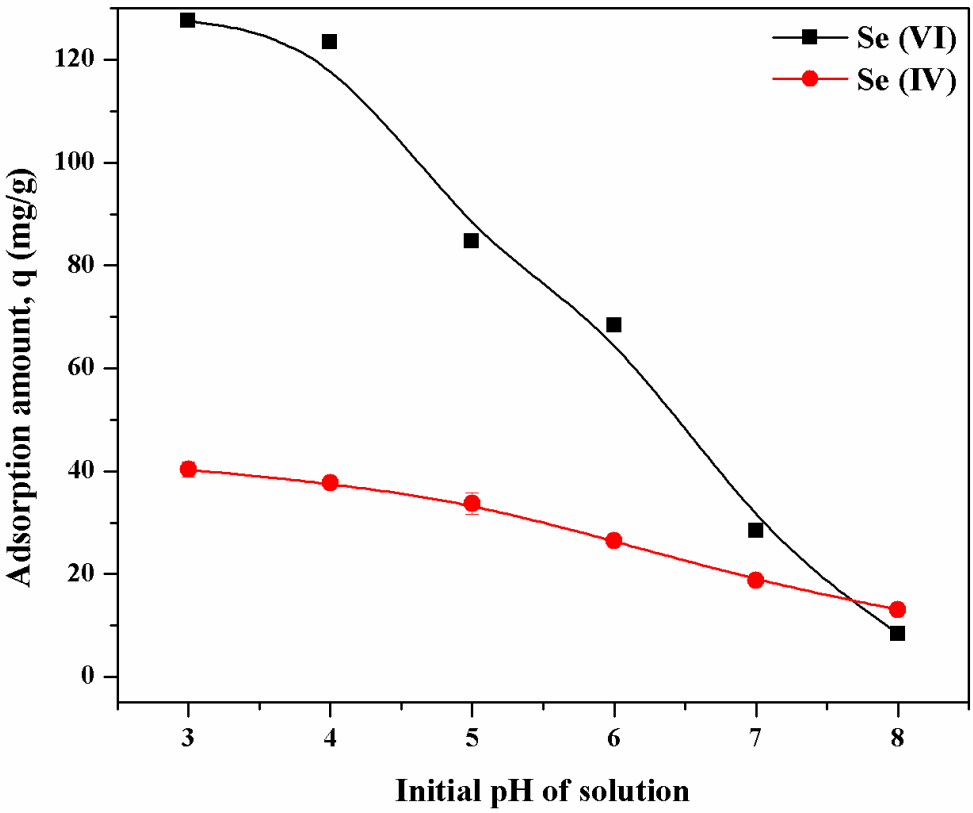

Figure 4-4 Effect of initial pH on selenium removal with initial Se concentration of 40 ppm.

4.5 Discussion of selenium adsorption mechanism

It is shown from the above results that PAMAM-GO, especially GO-G4, has good performance in the removal of both Se (IV) and Se (VI). Since initial pH of the solution has a great impact on the removal capacity of selenium, the adsorption of selenite and selenate ions on GO-G4 are considered to be mainly governed by electrostatic interactions. Zeta potential of GO-G4 was measured in 1 mM NaCl aqueous solution to explore possible mechanism for selenium

adsorption on dendrimer functionalized graphene oxide (shown in Figure 4-5). The zeta potential was found to decrease as pH increased, with an isoelectric point of 7.9. At low pH, more primary amine and tertiary amine groups are protonated, providing more active sites for binding negative-charged selenium ions. As the initial pH increases, these two kinds of amine groups become deprotonated, leading to the decrease of zeta-potential.

According to Eh-pH diagrams of the system Se-O-H,[5] it is obvious that selenite exists as the single charged anion ($HSeO_3^-$) below pH 7 while as the double charged anion (SeO_3^{2-}) above pH 7. On the other hand, selenate is presented as the double charged anion whenever the pH is larger than 2. In the adsorption process using GO-G4 as adsorbents, both Se (IV) and Se (VI) ions can be adsorbed by electrostatic attraction. At pH below 7, Se (VI) ions are more negative charged, resulting in stronger electrostatic attraction than Se (IV) ions with GO-G4. While at pH above 7, both Se (IV) and Se (VI) ions ionize completely, however, amine groups of GO-G4 become deprotonated and the electrostatic interactions become weaker. In that case, the removal capacities of selenium ions on GO-G4 decrease.

Compared to Se (VI), adsorption amount of Se (IV) is less impacted by initial pH, it can be attributed to the formation of an inner-sphere complex through aqueous ligand exchanging with the surface hydroxyl groups.[139-141] The decrease of the removal efficiency of Se (IV) from GO-G3 to GO-G4 (shown in Figure 4-1) can be attributed to larger dendrimer molecules that hinder selenium ions to interact with the basal plane of GO, leading to less ions adsorbed by ligand exchanging (illustrated in Figure 4-6).

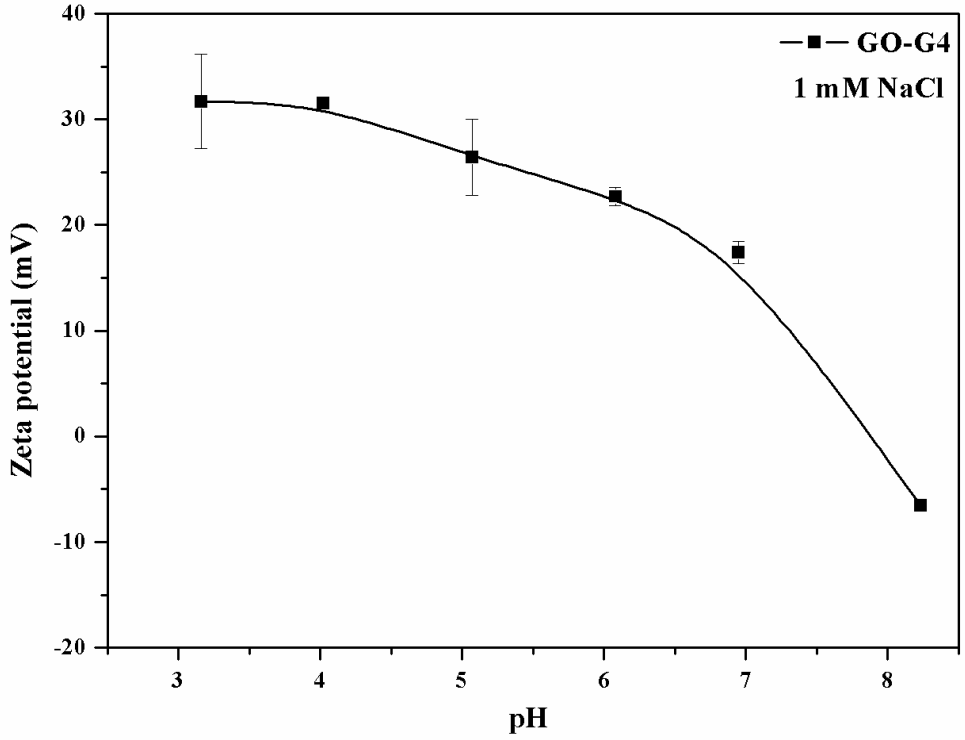

Figure 4-5 Zeta potential of GO-G4 as function of pH.

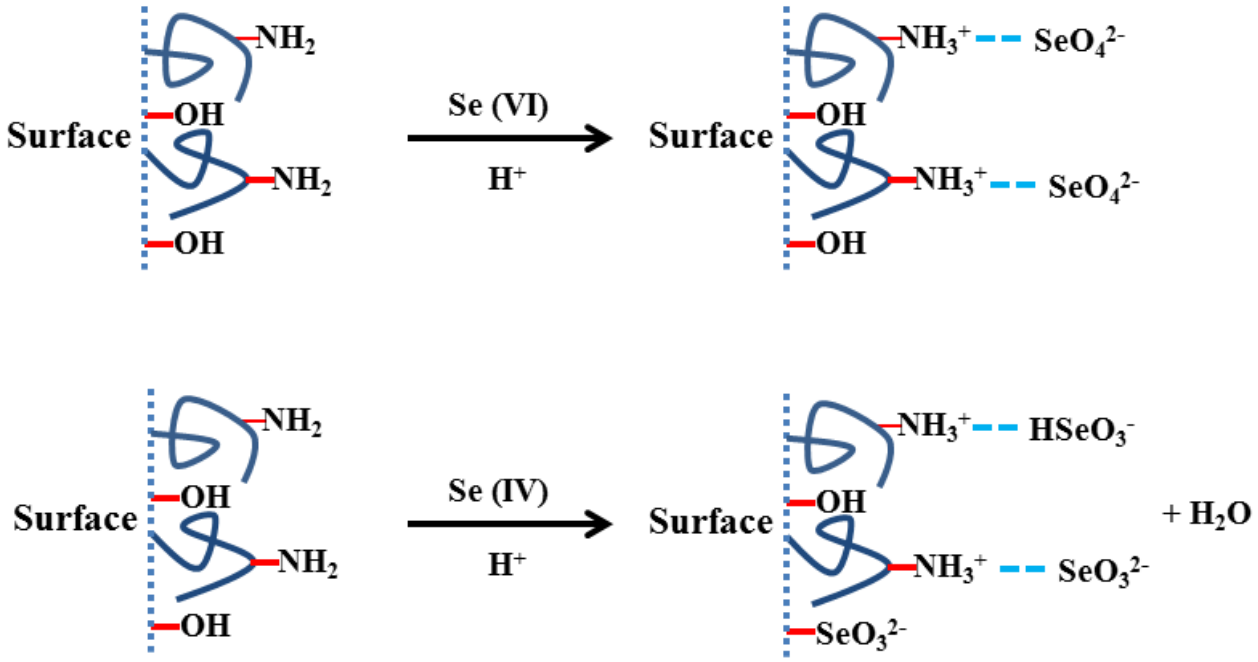

Figure 4-6 Schematic illustration of adsorption mechanisms for Se (IV) and Se (VI) on GO-G4.

Chapter 5 Preparation and Characterization of Dendrimer Functionalized Magnetic Graphene Oxide

Iron oxide has been applied in selenium removal[142-144] and the mechanism of selenium adsorption on iron oxide has been reported.[145-146] The adsorption of Se (VI) on goethite was well described by the modified triple-layer model, indicating Se (VI) was adsorbed via electrostatic attraction, forming outer-sphere surface complexes. On the contrary, Se (IV) forms two kinds of complexes during the adsorption process which are both inner-sphere surface complexes.[146] The inner-sphere surface complexes are more stable than outer-sphere surface complexes, which makes the adsorption of Se (IV) more efficient on iron oxide.

In this thesis, we reported a new kind of adsorbents that more efficient in Se (VI) removal. It is possible to improve the performance in both Se (IV) and Se (VI) removal by combining the magnetic iron oxide with PAMAM-GO to develop dendrimer functionalized magnetic graphene oxide (PAMAM-MGO). The combination could help stabilize iron oxide nanoparticles and provide more active sites for adsorption. Moreover, the adsorbents can be easily collected and recycled after magnetic separation and Se stripping at high pH. The primary results for the characterization of PAMAM-MGO are shown as follows:

The TEM images of graphene oxide and PAMAM-MGO are shown in Figure 5-1. Figure 5-1a shows that graphene oxide possesses a transparent sheet structure. The TEM images of PAMAM-MGO show that magnetic nanoparticles are well dispersed on the surface of GO nanosheets, with an average particle size of ~ 20 nm. Figure 5-1c shows a closer view of the designated area in Figure 5-1b.

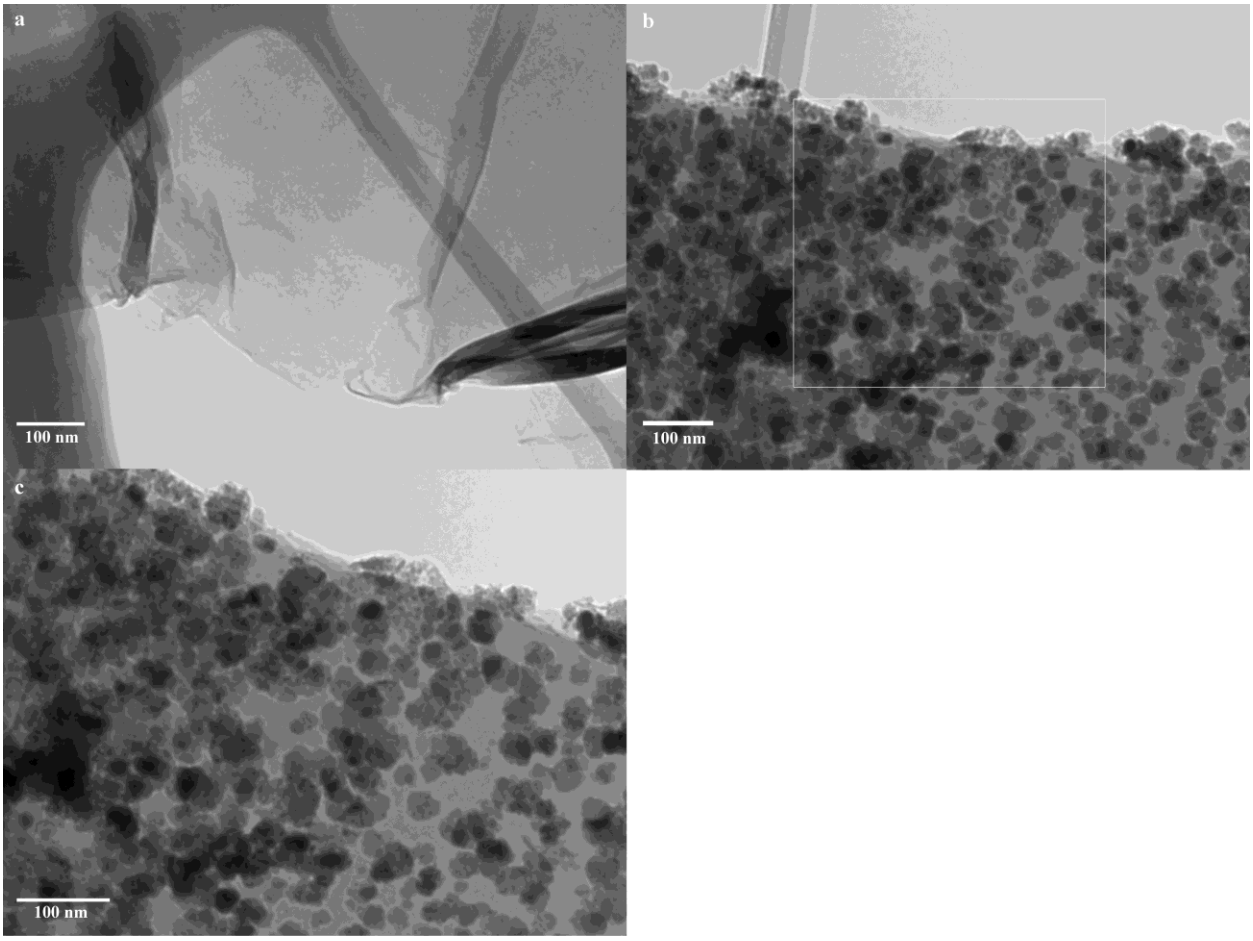

Figure 5-1 TEM images of (a) GO and (b), (c) PAMAM-MGO.

The Fourier Transform Infrared Spectroscopy (FTIR) spectra of GO, GO-G4 and PAMAM-MGO are shown in Figure 5-2. In the FTIR spectra of GO, the peaks observed at 1620 $cm^{-1}$and 1730 cm^{-1} indicate the presence of C=C and C=O, respectively. A broad peak at around 3200 cm^{-1} is also observed due to the presence of hydroxyl groups on the basal plane of GO. In the spectra of GO-G4 and PAMAM-MGO, the peaks observed at 2873 cm^{-1}, 2938 cm^{-1} and 2971 cm^{-1} are attributed to the asymmetric or symmetric stretch of C-H bond in methyl or methylene groups. The peak appeared at around 1550 cm^{-1} indicates the existence of amine groups on GO-G4 and PAMAM-MGO.

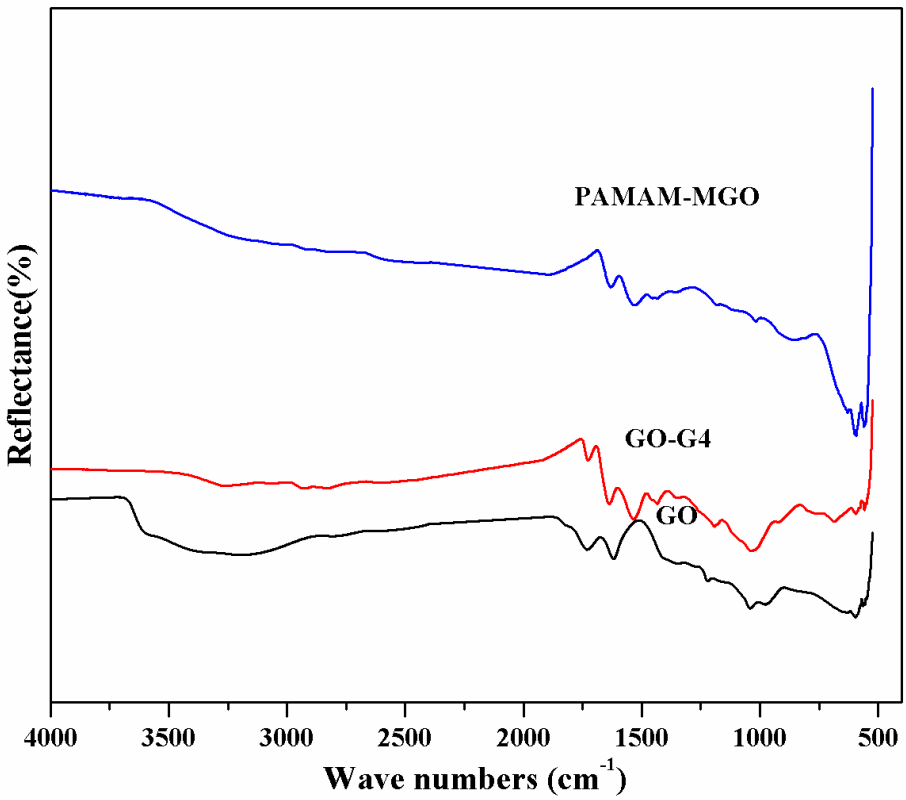

Figure 5-2 FTIR spectra of GO, GO-G4 and PAMAM-MGO.

The existence and structure of magnetic iron oxide particles were further determined by X-ray diffraction (XRD) patterns (shown in Figure 5-3). According to Bragg Equation ($2d\sin\theta=\lambda$, λ is the wavelength of X-ray, ~ 1.54 Å), the interlayer space of GO is 7.7 Å at $2\theta=11.4°$. The XRD pattern of GO-G4 shows a broad peak at $2\theta=15\text{-}35°$, indicating that the PAMAM-modified graphene oxide exist in a form of noncrystalline state.[130] In the XRD patterns of PAMAM-MGO, the characteristic peaks (2θ) at 30.1°, 35.5°, 43.1°, 53.4°, 57.0° and 62.6° are consistent with the standard patterns of magnetite, which proves the existence of magnetic particles on the surface of graphene oxide.

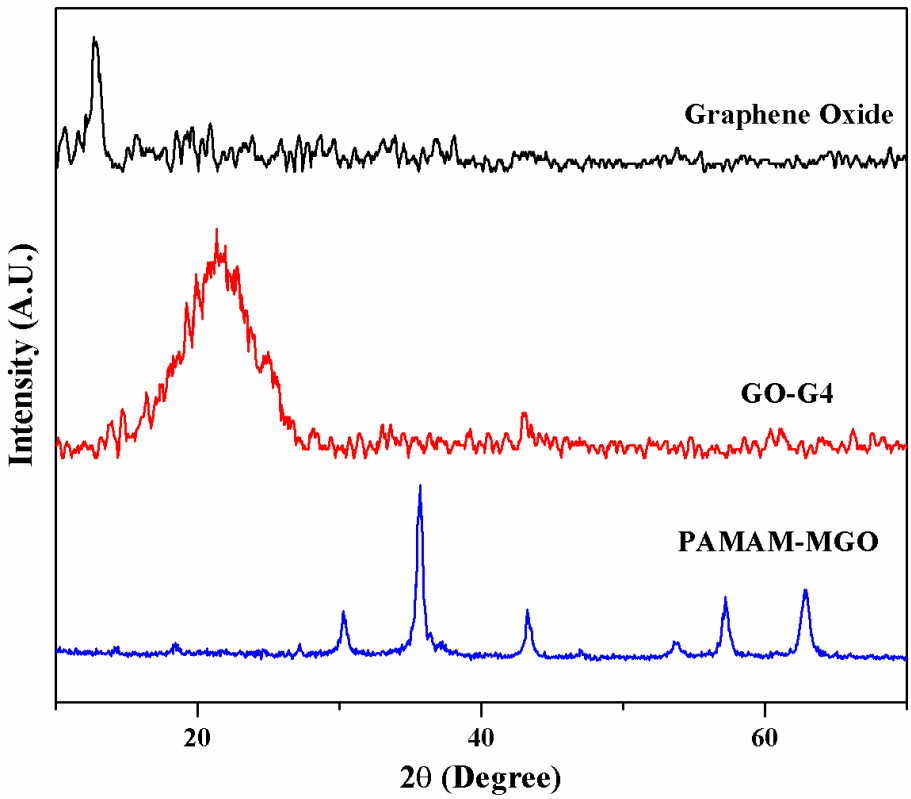

Figure 5-3 X-ray diffraction patterns of GO, GO-G4 and PAMAM-MGO.

The TGA curves of GO, GO-G4 and PAMAM-MGO are shown in Figure 5-4. For GO, the weight loss started from ~ 20 °C to ~ 120 °C could be attributed to adsorbed water. The most significant weight loss occurs at around 160 °C, which may be due to pyrolysis of the labile oxygen-containing functional groups, yielding CO, CO_2, and steam.[131-132] The further mass loss starting at around 600 °C is attributed to the pyrolysis of the carbon skeleton of GO.[133] The TGA curve of GO-G4 shows a significant weight loss starting at around 280 °C, which is attributed to the decomposition of PAMAM dendrimers.[134-135] Compared to the GO and GO-G4, PAMAM-

MGO gradually loses weight due to the lower weight percentage of GO and the oxidization of Fe_3O_4 to γ-Fe_2O_3.[147]

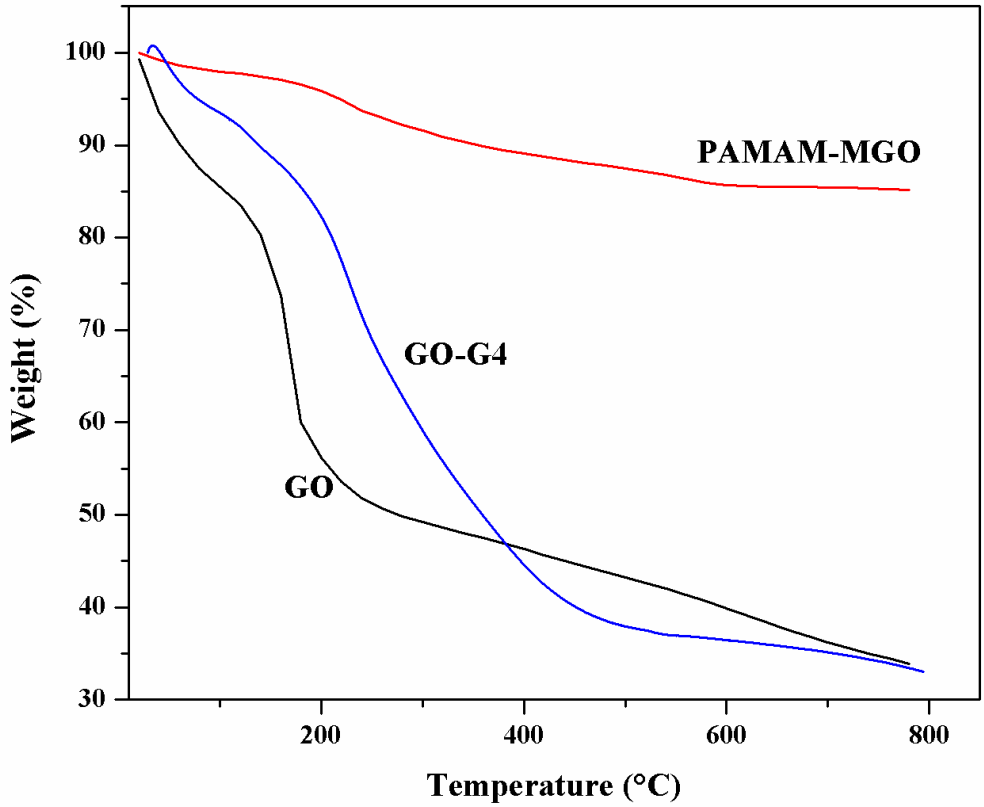

Figure 5-4 TGA curves of GO, GO-G4 and PAMAM-MGO.

Magnetic measurement of PAMAM-MGO was carried out at room temperature. As shown in Figure 5-5, the saturation magnetization is 57.7 emu g^{-1}, which is lower than reported value (92 emu g^{-1}) of pure iron oxide nanocrystals.[148] This can be explained by the presence of graphene oxide and PAMAM. In addition, PAMAM-MGO exhibits no remanence effect at low applied magnetic fields (shown in the inset in Figure 5-5). The magnetic properties will enhance the application by rapid separation from the solutions when applied magnetic fields.

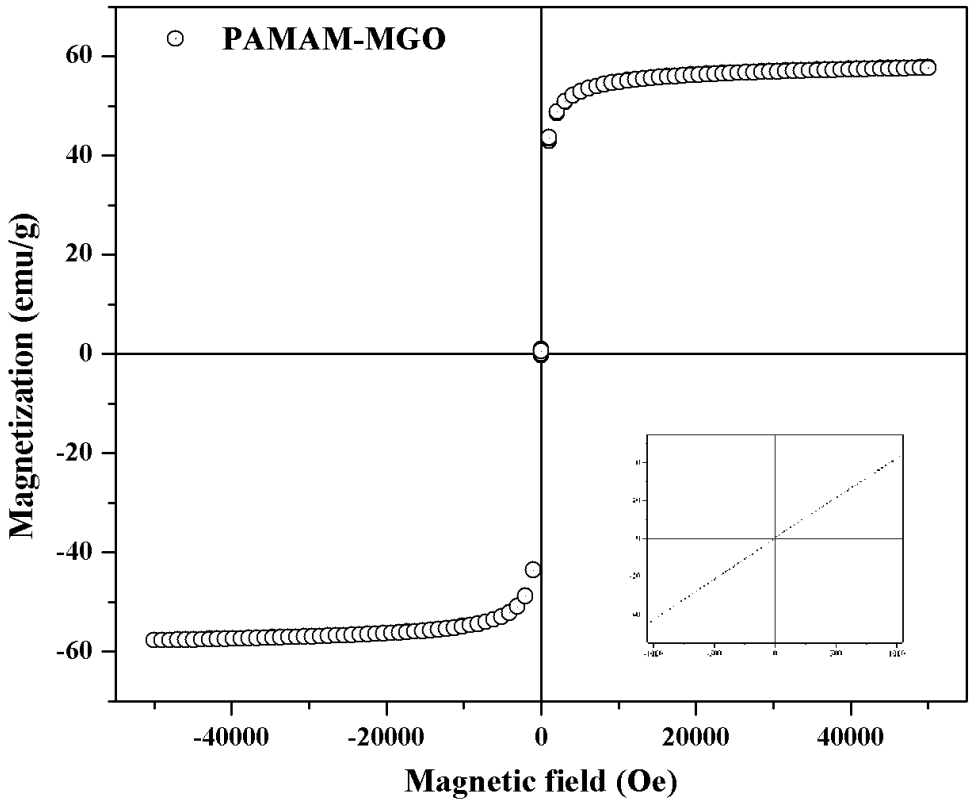

Figure 5-5 Magnetization curve of PAMAM-MGO at room temperature. Inset is a magnified view of the magnetization curve at low applied fields.

Chapter 6 Conclusions, Contributions and Future Work

6.1 Conclusions

Selenium has been a challenging environment issue. Various adsorbents have been applied for the removal of selenium from water but did not show good performance, especially in Se (VI) removal, which is more bioavailable and more difficult to remove. In this project, different generations of dendrimer functionalized graphene oxide (PAMAM-GO) were synthesized and applied for the removal of selenium ions from water. Our results show that the removal capacities of Se (IV) and Se (VI) ions increase with the generation of PAMAM-GO. Compared to GO and MGO, GO-G4 has good performance in the removal of both Se (IV) and Se (VI) with capacities 60.9 mg g^{-1} and 77.9 mg g^{-1} at pH 6. This work provides new technology and insight for selenium removal from aqueous environment.

The conclusions in this work are summarized as follows:

(1) Different generations of dendrimer functionalized graphene oxide (PAMAM-GO) were prepared using a new method via silanization of GO, followed by Michael addition reaction and amidation of ester groups.

(2) PAMAM-GO were characterized by TEM, FTIR, XPS, XRD, TGA, etc for surface morphologies analysis and chemical compositions analysis. TEM images showed different surface features of GO-G4, compared to GO, which should be attributed to dendrimer molecules grafted onto the surface of GO. FTIR, XPS and XRD characterized the chemical compositions and structures of different generations of PAMAM-GO, indicating the successful functionalization of PAMAM molecules onto the surface of GO.

(3) In selenium adsorption tests, different generations of PAMAM-GO show high removal capabilities for selenite and selenate. GO-G4 shows higher adsorption capability of Se (VI) than Se (IV), with a removal capacity of 60.9 mg g^{-1} in Se (IV) and 77.9 mg g^{-1} in Se (VI) at pH 6.

(4) The removal capacities of selenium ions on PAMAM-GO can be impacted by adsorption conditions such as generations of dendrimer and initial pH. Our results show an increase from GO-G0 to GO-G4 in the removal capacities of Se (VI) on PAMAM-GO while a decrease from GO-G3 to GO-G4 in the removal capacities of Se (IV). Lower initial pH can facilitate the adsorption process of both selenium ions on GO-G4, with a greater influence on the removal of selenate than selenite. When applying GO-G4 as adsorbent, the removal capacity of Se (VI) increased to a capacity of 127 mg g^{-1} at pH = 3 while that of Se (IV) increased to a capacity of 39 mg g^{-1}.

(5) Adsorption of Se (IV) and Se (VI) on GO, MGO, GO-G4 were also compared in this work. GO-G4 showed a better performance in both Se (IV) and Se (VI) removal, especially for the removal of selenate.

(6) The adsorption of Se (VI) on GO-G4 is attributed to the electrostatic interaction between charged amine groups and double charged selenate anions. On the contrary, the mechanism of the adsorption of Se (IV) on GO-G4 could be a combination of electrostatic interaction between charged amine groups and selenite anions and the formation of an inner-sphere complex through ligand exchanging with hydroxyl groups on the surface of GO.

6.2 Contributions to the original knowledge

In this work, different generations of dendrimer functionalized graphene oxide (PAMAM-GO) were prepared using a new method via silanization of GO, followed by Michael addition reaction and amidation of ester groups. The resulting materials were applied for the removal of selenium ions from water. Previously reported adsorbents performed well in Se (IV) removal rather than Se (VI), which is more toxic for human. However, PAMAM-GO, especially for the 4^{th} generation, GO-G4, shows a much better performance in both selenium oxyanions removal and higher adsorption capability in Se (VI) removal. The results show that PAMAM-GO has an excellent performance in selenium removal from waste water and provide a new scope on adsorbents for selenium removal.

6.3 Future work

6.3.1 Effects of ion strength on selenite and selenate removal

As discussed above, selenium adsorption occurs in two different ways: electrostatic interactions and ligand exchange. The adsorption of Se (VI) on PAMAM-GO is attributed to electrostatic attraction between SeO_4^{2-} and protonated amine groups. The adsorption will be affected by ion strength. However, Se (IV) is assumed to be adsorbed on PAMAM-GO via both electrostatic attraction and ligand exchange.

Indicated in previous research, selenate adsorption is strongly affected by ion strength while selenite adsorption is relatively unaffected by the changes in ion strength. By studying the effects of ion strength on both selenium ions removal, it is possible to figure out the adsorption

mechanisms of both selenium ions on PAMAM-GO and they can be further confirmed by infrared spectroscopy study.[139-140]

6.3.2 Interfering ions

Selenium oxyanions removal could be effected by interfering ions, including SO_4^{2-} and PO_4^{3-}.[149] The effects of these interfering ions will be further studied under different ion concentrations, pH and ion strength. Pre-treatment methods will be developed for highly interfering ions in further work, as well as the consideration of total cost.

6.3.3 Potential applications for pollutants removal

As mentioned in the literature review, PAMAM-GO can be applied in various pollutants removal, including Hg (II), Zn (II) and CO_2. It is feasible to considerate PAMAM-GO as a universal adsorbent for different pollutants removal in the industry.

Bibliography

1. WHO, Guidelines for Drinking-water Quality. 2011.

2. Wilber, C. G., Toxicology of Selenium - a Review. *Clin Toxicol* **1980,** *17* (2), 171-230.

3. Thomas M. Miller; Goodman, W. H. Removal of selenium from water by complexation with polymeric dithiocarbamates. 1996.

4. Smith, K.; Lau, A. O.; Vance, F. W., Evaluation of Treatment Techniques for Selenium Removal. *IWC 09-05*.

5. Takeno, N., Atlas of Eh-pH diagrams. Intercomparison of Thermodynamic Databases. Geological Survey of Japan Open File Report File No. 419. National Institute of Advanced Industrial Science and Technology. *Research Center for Deep Geological Environments* **2005**.

6. Merrill, D. T.; Manzione, M. A.; Peterson, J. J.; Parker, D. S.; Chow, W.; Hobbs, A. O., Field-Evaluation of Arsenic and Selenium Removal by Iron Coprecipitation. *J Water Pollut Con F* **1986,** *58* (1), 18-26.

7. Moody, C. D.; Murphy, A. P., Selenium Removal with Ferrous Hydroxide - Identification of Competing and Interfering Solutes. *Toxic Substances in Agricultural Water Supply and Drainage* **1989**, 231-246.

8. Murphy, A. P., A Water-Treatment Process for Selenium Removal. *J Water Pollut Con F* **1989,** *61* (3), 361-362.

9. Tam, S. C.; Chow, A.; Hadley, D., Effects of Organic-Component on the Immobilization of Selenium on Iron Oxyhydroxide. *Sci Total Environ* **1995,** *164* (1), 1-7.

10. Liao, M. Y.; Randtke, S. J., Predicting the Removal of Soluble Organic Contaminants by Lime Softening. *Water Res* **1986,** *20* (1), 27-35.

11. Nishimura, T.; Hashimoto, H.; Nakayama, M., Removal of selenium(VI) from aqueous solution with polyamine-type weakly basic ion exchange resin. *Separ Sci Technol* **2007,** *42* (14), 3155-3167.

12. Hocquellet, P.; Candillier, M. P., Evaluation of Microwave Digestion and Solvent-Extraction for the Determination of Trace Amounts of Selenium in Feeds and Plant and Animal-Tissues by Electrothermal Atomic-Absorption Spectrometry. *Analyst* **1991,** *116* (5), 505-509.

13. Chambers, J. C.; Mcclellan, B. E., Enhancement of Atomic-Absorption Sensitivity for Copper, Cadmium, Antimony, Arsenic, and Selenium by Means of Solvent-Extraction. *Anal Chem* **1976,** *48* (14), 2061-2066.

14. Marinas, B. J.; Selleck, R. E., Reverse-Osmosis Treatment of Multicomponent Electrolyte-Solutions. *J Membrane Sci* **1992,** *72* (3), 211-229.

15. Gleason, K. J.; Yu, J. H.; Bunge, A. L.; Wright, J. D., Removal of selenium from contaminated waters using emulsion liquid membranes. *Acs Sym Ser* **1996,** *642*, 342-360.

16. Kharaka, Y. K.; Ambats, G.; Presser, T. S.; Davis, R. A., Removal of selenium from contaminated agricultural drainage water by nanofiltration membranes. *Appl Geochem* **1996,** *11* (6), 797-802.

17. Hockin, S. L.; Gadd, G. M., Linked redox precipitation of sulfur and selenium under anaerobic conditions by sulfate-reducing bacterial biofilms. *Appl Environ Microb* **2003,** *69* (12), 7063-7072.

18. Yang, H.; Xu, R.; Xue, X. M.; Li, F. T.; Li, G. T., Hybrid surfactant-templated mesoporous silica formed in ethanol and its application for heavy metal removal. *J Hazard Mater* **2008,** *152* (2), 690-698.

19. Kadirvelu, K.; Faur-Brasquet, C.; Le Cloirec, P., Removal of Cu(II), Pb(II), and Ni(II) by adsorption onto activated carbon cloths. *Langmuir* **2000,** *16* (22), 8404-8409.

20. Genz, A.; Kornmuller, A.; Jekel, M., Advanced phosphorus removal from membrane filtrates by adsorption on activated aluminium oxide and granulated ferric hydroxide. *Water Res* **2004,** *38* (16), 3523-3530.

21. Erdem, E.; Karapinar, N.; Donat, R., The removal of heavy metal cations by natural zeolites. *J Colloid Interf Sci* **2004,** *280* (2), 309-314.

22. Izatt, R. M.; Bruening, R. L.; Bruening, M. L.; Tarbet, B. J.; Krakowiak, K. E.; Bradshaw, J. S.; Christensen, J. J., Removal and Separation of Metal-Ions from Aqueous-Solutions Using a Silica-Gel-Bonded Macrocycle System. *Anal Chem* **1988,** *60* (17), 1825-1826.

23. Panday, K. K.; Prasad, G.; Singh, V. N., Copper(Ii) Removal from Aqueous-Solutions by Fly-Ash. *Water Res* **1985,** *19* (7), 869-873.

24. Fu, F. L.; Wang, Q., Removal of heavy metal ions from wastewaters: A review. *J Environ Manage* **2011,** *92* (3), 407-418.

25. Ruthven, D. M., Principles of adsorption and adsorption processes. **1984**.

26. Twidwell, L. G., The removal of arsenic, selenium and metals from aqueous solution by iron precipitation and reduction techniques. *presented at TMS2011 Annual Meeting, San Diego, CA* **2011**.

27. Tomalia, D. A.; Baker, H.; Dewald, J.; Hall, M.; Kallos, G.; Martin, S.; Roeck, J.; Ryder, J.; Smith, P., A New Class of Polymers - Starburst-Dendritic Macromolecules. *Polym J* **1985,** *17* (1), 117-132.

28. Klajnert, B.; Bryszewska, M., Dendrimers: properties and applications. *Acta Biochim Pol* **2001,** *48* (1), 199-208.

29. Hawker, C. J.; Frechet, J. M. J., Preparation of Polymers with Controlled Molecular Architecture - a New Convergent Approach to Dendritic Macromolecules. *J Am Chem Soc* **1990,** *112* (21), 7638-7647.

30. Hodge, P., Organic-Chemistry - Polymer Science Branches Out. *Nature* **1993,** *362* (6415), 18-19.

31. Alper, J., Rising Chemical Stars Could Play Many Roles. *Science* **1991,** *251* (5001), 1562-1564.

32. Zhuo, R. X.; Du, B.; Lu, Z. R., In vitro release of 5-fluorouracil with cyclic core dendritic polymer. *J Control Release* **1999,** *57* (3), 249-257.

33. Bielinska, A.; KukowskaLatallo, J. F.; Johnson, J.; Tomalia, D. A.; Baker, J. R., Regulation of in vitro gene expression using antisense oligonucleotides or antisense expression plasmids transfected using starburst PAMAM dendrimers. *Nucleic Acids Res* **1996,** *24* (11), 2176-2182.

34. Tomalia, D.; Dvornic, P. R., Catalysis - What Promise for Dendrimers. *Nature* **1994,** *372* (6507), 617-618.

35. Rahim, E. H.; Kamounah, F. S.; Frederiksen, J.; Christensen, J. B., Heck reactions catalyzed by PAMAM-dendrimer encapsulated Pd(0) nanoparticles. *Nano Lett* **2001,** *1* (9), 499-501.

36. Fadhel, B.; Hearn, M.; Chaffee, A., CO2 adsorption by PAMAM dendrimers: Significant effect of impregnation into SBA-15. *Micropor Mesopor Mat* **2009,** *123* (1-3), 140-149.

37. Ma, F.; Qu, R. J.; Sun, C. M.; Wang, C. H.; Ji, C. N.; Zhang, Y.; Yin, P., Adsorption behaviors of Hg(II) on chitosan functionalized by amino-terminated hyperbranched polyamidoamine polymers. *J Hazard Mater* **2009,** *172* (2-3), 792-801.

38. Chou, C. M.; Lien, H. L., Dendrimer-conjugated magnetic nanoparticles for removal of zinc (II) from aqueous solutions. *J Nanopart Res* **2011,** *13* (5), 2099-2107.

39. Zhang, Y. B.; Tan, Y. W.; Stormer, H. L.; Kim, P., Experimental observation of the quantum Hall effect and Berry's phase in graphene. *Nature* **2005,** *438* (7065), 201-204.

40. Kroto, H. W.; Allaf, A. W.; Balm, S. P., C60 - Buckminsterfullerene. *Chem Rev* **1991,** *91* (6), 1213-1235.

41. Iijima, S., Helical Microtubules of Graphitic Carbon. *Nature* **1991,** *354* (6348), 56-58.

42. Novoselov, K. S.; Geim, A. K.; Morozov, S. V.; Jiang, D.; Zhang, Y.; Dubonos, S. V.; Grigorieva, I. V.; Firsov, A. A., Electric field effect in atomically thin carbon films. *Science* **2004,** *306* (5696), 666-669.

43. Geim, A. K.; Novoselov, K. S., The rise of graphene. *Nat Mater* **2007,** *6* (3), 183-191.

44. Chae, H. K.; Siberio-Perez, D. Y.; Kim, J.; Go, Y.; Eddaoudi, M.; Matzger, A. J.; O'Keeffe, M.; Yaghi, O. M., A route to high surface area, porosity and inclusion of large molecules in crystals. *Nature* **2004,** *427* (6974), 523-527.

45. Schadler, L. S.; Giannaris, S. C.; Ajayan, P. M., Load transfer in carbon nanotube epoxy composites. *Appl Phys Lett* **1998,** *73* (26), 3842-3844.

46. Novoselov, K. S.; Geim, A. K.; Morozov, S. V.; Jiang, D.; Katsnelson, M. I.; Grigorieva, I. V.; Dubonos, S. V.; Firsov, A. A., Two-dimensional gas of massless Dirac fermions in graphene. *Nature* **2005,** *438* (7065), 197-200.

47. Novoselov, K. S.; McCann, E.; Morozov, S. V.; Fal'ko, V. I.; Katsnelson, M. I.; Zeitler, U.; Jiang, D.; Schedin, F.; Geim, A. K., Unconventional quantum Hall effect and Berry's phase of 2 pi in bilayer graphene. *Nat Phys* **2006,** *2* (3), 177-180.

48. Katsnelson, M. I.; Novoselov, K. S.; Geim, A. K., Chiral tunnelling and the Klein paradox in graphene. *Nat Phys* **2006,** *2* (9), 620-625.

49. Geim, A. K., Graphene: Status and Prospects. *Science* **2009,** *324* (5934), 1530-1534.

50. Brodie, B. C., On the Atomic Weight of Graphite. *Philosophical Transactions of Royal Society of London* **1859,** *149*, 249-259.

51. Staudenmaier, L., Verfahren zur Darstellung der Graphitsäure. *Berichte der deutschen chemischen Gesellschaft* **1898,** *31*, 1481–1487.

52. Hummers, W. S.; Offeman, R. E., Preparation of Graphitic Oxide. *J Am Chem Soc* **1958,** *80* (6), 1339-1339.

53. Tang, Q.; Zhou, Z.; Chen, Z. F., Graphene-related nanomaterials: tuning properties by functionalization. *Nanoscale* **2013,** *5* (11), 4541-4583.

54. Wang, L.; Lee, K.; Sun, Y. Y.; Lucking, M.; Chen, Z. F.; Zhao, J. J.; Zhang, S. B. B., Graphene Oxide as an Ideal Substrate for Hydrogen Storage. *Acs Nano* **2009,** *3* (10), 2995-3000.

55. Li, F. Y.; Zhao, J. J.; Chen, Z. F., Fe-Anchored Graphene Oxide: A Low-Cost and Easily Accessible Catalyst for Low-Temperature CO Oxidation. *J Phys Chem C* **2012,** *116* (3), 2507-2514.

56. Chang, H. X.; Wu, H. K., Graphene-based nanocomposites: preparation, functionalization, and energy and environmental applications. *Energ Environ Sci* **2013,** *6* (12), 3483-3507.

57. Xu, Y. X.; Bai, H.; Lu, G. W.; Li, C.; Shi, G. Q., Flexible graphene films via the filtration of water-soluble noncovalent functionalized graphene sheets. *J Am Chem Soc* **2008,** *130* (18), 5856-+.

58. Yang, X. Y.; Zhang, X. Y.; Liu, Z. F.; Ma, Y. F.; Huang, Y.; Chen, Y., High-Efficiency Loading and Controlled Release of Doxorubicin Hydrochloride on Graphene Oxide. *J Phys Chem C* **2008,** *112* (45), 17554-17558.

59. Qi, X. Y.; Pu, K. Y.; Li, H.; Zhou, X. Z.; Wu, S. X.; Fan, Q. L.; Liu, B.; Boey, F.; Huang, W.; Zhang, H., Amphiphilic Graphene Composites. *Angew Chem Int Edit* **2010,** *49* (49), 9426-9429.

60. Choi, E. Y.; Han, T. H.; Hong, J. H.; Kim, J. E.; Lee, S. H.; Kim, H. W.; Kim, S. O., Noncovalent functionalization of graphene with end-functional polymers. *J Mater Chem* **2010,** *20* (10), 1907-1912.

61. Stankovich, S.; Piner, R. D.; Nguyen, S. T.; Ruoff, R. S., Synthesis and exfoliation of isocyanate-treated graphene oxide nanoplatelets. *Carbon* **2006,** *44* (15), 3342-3347.

62. Veca, L. M.; Lu, F. S.; Meziani, M. J.; Cao, L.; Zhang, P. Y.; Qi, G.; Qu, L. W.; Shrestha, M.; Sun, Y. P., Polymer functionalization and solubilization of carbon nanosheets. *Chem Commun* **2009,** (18), 2565-2567.

63. Xu, Y. F.; Liu, Z. B.; Zhang, X. L.; Wang, Y.; Tian, J. G.; Huang, Y.; Ma, Y. F.; Zhang, X. Y.; Chen, Y. S., A Graphene Hybrid Material Covalently Functionalized with Porphyrin: Synthesis and Optical Limiting Property. *Adv Mater* **2009,** *21* (12), 1275-+.

64. Yang, H. F.; Shan, C. S.; Li, F. H.; Han, D. X.; Zhang, Q. X.; Niu, L., Covalent functionalization of polydisperse chemically-converted graphene sheets with amine-terminated ionic liquid. *Chem Commun* **2009,** (26), 3880-3882.

65. Wan, Y. J.; Gong, L. X.; Tang, L. C.; Wu, L. B.; Jiang, J. X., Mechanical properties of epoxy composites filled with silane-functionalized graphene oxide. *Compos Part a-Appl S* **2014,** *64*, 79-89.

66. Meric, I.; Han, M. Y.; Young, A. F.; Ozyilmaz, B.; Kim, P.; Shepard, K. L., Current saturation in zero-bandgap, topgated graphene field-effect transistors. *Nat Nanotechnol* **2008,** *3* (11), 654-659.

67. Yu, J. G.; Yu, L. Y.; Yang, H.; Liu, Q.; Chen, X. H.; Jiang, X. Y.; Chen, X. Q.; Jiao, F. P., Graphene nanosheets as novel adsorbents in adsorption, preconcentration and removal of gases, organic compounds and metal ions. *Sci Total Environ* **2015,** *502*, 70-79.

68. An, X. Q.; Yu, X. L.; Yu, J. C.; Zhang, G. J., CdS nanorods/reduced graphene oxide nanocomposites for photocatalysis and electrochemical sensing. *J Mater Chem A* **2013,** *1* (16), 5158-5164.

69. Wang, Z. H.; Du, Y. L.; Zhang, F. Y.; Zheng, Z. X.; Zhang, X. L.; Feng, Q. L.; Wang, C. M., Photocatalytic degradation of pendimethalin over Cu2O/SnO2/graphene and SnO2/graphene nanocomposite photocatalysts under visible light irradiation. *Mater Chem Phys* **2013,** *140* (1), 373-381.

70. Rajeshwar, K.; Osugi, M. E.; Chanmanee, W.; Chenthamarakshan, C. R.; Zanoni, M. V. B.; Kajitvichyanukul, P.; Krishnan-Ayer, R., Heterogeneous photocatalytic treatment of organic dyes in air and aqueous media. *J Photoch Photobio C* **2008,** *9* (4), 171-192.

71. Zhang, H.; Lv, X. J.; Li, Y. M.; Wang, Y.; Li, J. H., P25-Graphene Composite as a High Performance Photocatalyst. *Acs Nano* **2010,** *4* (1), 380-386.

72. Kyzas, G. Z.; Deliyanni, E. A.; Matis, K. A., Graphene oxide and its application as an adsorbent for wastewater treatment. *J Chem Technol Biot* **2014,** *89* (2), 196-205.

73. Romero, H. E.; Joshi, P.; Gupta, A. K.; Gutierrez, H. R.; Cole, M. W.; Tadigadapa, S. A.; Eklund, P. C., Adsorption of ammonia on graphene. *Nanotechnology* **2009,** *20* (24).

74. Paulus, B.; Rosciszewski, K., Application of the Method of Increments to the Adsorption of H2S on Graphene. *Int J Quantum Chem* **2009,** *109* (13), 3055-3062.

75. Terzyk, A. P.; Furmaniak, S.; Gauden, P. A.; Kowalczyk, P., Fullerene-intercalated Graphene Nano-containers - Mechanism of Argon Adsorption and High-pressure CH4 and CO2 Storage Capacities. *Adsorpt Sci Technol* **2009,** *27* (3), 281-296.

76. Radovic, L. R.; Suarez, A.; Vallejos-Burgos, F.; Sofo, J. O., Oxygen migration on the graphene surface. 2. Thermochemistry of basal-plane diffusion (hopping). *Carbon* **2011,** *49* (13), 4226-4238.

77. Dai, J. Y.; Yuan, J. M.; Giannozzi, P., Gas adsorption on graphene doped with B, N, Al, and S: A theoretical study. *Appl Phys Lett* **2009,** *95* (23).

78. Gao, Y.; Li, Y.; Zhang, L.; Huang, H.; Hu, J. J.; Shah, S. M.; Su, X. G., Adsorption and removal of tetracycline antibiotics from aqueous solution by graphene oxide. *J Colloid Interf Sci* **2012,** *368*, 540-546.

79. Pei, Z. G.; Li, L. Y.; Sun, L. X.; Zhang, S. Z.; Shan, X. Q.; Yang, S.; Wen, B., Adsorption characteristics of 1,2,4-trichlorobenzene, 2,4,6-trichlorophenol, 2-naphthol and naphthalene on graphene and graphene oxide. *Carbon* **2013,** *51*, 156-163.

80. Li, L. L.; Fan, L. L.; Sun, M.; Qiu, H. M.; Li, X. J.; Duan, H. M.; Luo, C. N., Adsorbent for hydroquinone removal based on graphene oxide functionalized with magnetic cyclodextrin-chitosan. *Int J Biol Macromol* **2013,** *58*, 169-175.

81. Ren, X. M.; Li, J. X.; Tan, X. L.; Wang, X. K., Comparative study of graphene oxide, activated carbon and carbon nanotubes as adsorbents for copper decontamination. *Dalton T* **2013,** *42* (15), 5266-5274.

82. Zhao, G. X.; Li, J. X.; Ren, X. M.; Chen, C. L.; Wang, X. K., Few-Layered Graphene Oxide Nanosheets As Superior Sorbents for Heavy Metal Ion Pollution Management. *Environ Sci Technol* **2011,** *45* (24), 10454-10462.

83. Zhao, G. X.; Ren, X. M.; Gao, X.; Tan, X. L.; Li, J. X.; Chen, C. L.; Huang, Y. Y.; Wang, X. K., Removal of Pb(II) ions from aqueous solutions on few-layered graphene oxide nanosheets. *Dalton T* **2011,** *40* (41), 10945-10952.

84. Madadrang, C. J.; Kim, H. Y.; Gao, G. H.; Wang, N.; Zhu, J.; Feng, H.; Gorring, M.; Kasner, M. L.; Hou, S. F., Adsorption Behavior of EDTA-Graphene Oxide for Pb (II) Removal. *Acs Appl Mater Inter* **2012,** *4* (3), 1186-1193.

85. Musico, Y. L. F.; Santos, C. M.; Dalida, M. L. P.; Rodrigues, D. F., Improved removal of lead(II) from water using a polymer-based graphene oxide nanocomposite. *J Mater Chem A* **2013,** *1* (11), 3789-3796.

86. Liu, M. C.; Chen, C. L.; Hu, J.; Wu, X. L.; Wang, X. K., Synthesis of Magnetite/Graphene Oxide Composite and Application for Cobalt(II) Removal. *J Phys Chem C* **2011,** *115* (51), 25234-25240.

87. Sheng, G. D.; Li, Y. M.; Yang, X.; Ren, X. M.; Yang, S. T.; Hu, J.; Wang, X. K., Efficient removal of arsenate by versatile magnetic graphene oxide composites. *Rsc Adv* **2012,** *2* (32), 12400-12407.

88. Fan, L. L.; Luo, C. N.; Sun, M.; Li, X. J.; Qiu, H. M., Highly selective adsorption of lead ions by water-dispersible magnetic chitosan/graphene oxide composites. *Colloid Surface B* **2013,** *103*, 523-529.

89. Freundlich, H., Concerning adsorption in solutions. *Z Phys Chem-Stoch Ve* **1906,** *57* (4), 385-470.

90. Langmuir, I., The Adsorption of Gases on Plane Surfaces of Glass, Mica and Platinum. *J Am Chem Soc* **1918,** *40*, 1361-1403.

91. Valcarcel, M.; Cardenas, S.; Simonet, B. M.; Moliner-Martinez, Y.; Lucena, R., Carbon nanostructures as sorbent materials in analytical processes. *Trac-Trend Anal Chem* **2008,** *27* (1), 34-43.

92. Sitko, R.; Zawisza, B.; Malicka, E., Graphene as a new sorbent in analytical chemistry. *Trac-Trend Anal Chem* **2013,** *51*, 33-43.

93. Sorg, T. J.; Logsdon, G. S., Treatment Technology to Meet Interim Primary Drinking-Water Regulations for Inorganics .2. *J Am Water Works Ass* **1978,** *70* (7), 379-393.

94. Paek, S. M.; Yoo, E.; Honma, I., Enhanced Cyclic Performance and Lithium Storage Capacity of SnO2/Graphene Nanoporous Electrodes with Three-Dimensionally Delaminated Flexible Structure. *Nano Lett* **2009,** *9* (1), 72-75.

95. Pan, B. F.; Gao, F.; Gu, H. C., Dendrimer modified magnetite nanoparticles for protein immobilization. *J Colloid Interf Sci* **2005,** *284* (1), 1-6.

96. Tajabadi, M.; Khosroshahi, M. E.; Bonakdar, S., An efficient method of SPION synthesis coated with third generation PAMAM dendrimer. *Colloid Surface A* **2013,** *431*, 18-26.

97. Fultz, B.; Howe, J., *Transmission Electron Microscopy and Diffractometry of Materials* **2007**.

98. Bajt, S.; Barty, A.; Nugent, K. A.; McCartney, M.; Wall, M.; Paganin, D., Quantitative phase-sensitive imaging in a transmission electron microscope. *Ultramicroscopy* **2000,** *83* (1-2), 67-73.

99. Reimer, L.; Kohl, H., *Transmission electron microscopy: physics of image formation* **2008**.

100. Williams, D. B.; Carter, C. B., *The Transmission Electron Microscope* **1996**.

101. Michler, G. H., Electron Microscopy of Polymers. 2008.

102. Steiner, G.; Koch, E., Trends in Fourier transform infrared spectroscopic imaging. *Anal Bioanal Chem* **2009,** *394* (3), 671-678.

103. Simonescu, C. M., Application of FTIR Spectroscopy in Environmental Studies. *Advanced Aspects of Spectroscopy, Chapter 2* **2012**.

104. Berthomieu, C.; Hienerwadel, R., Fourier transform infrared (FTIR) spectroscopy. *Photosynth Res* **2009,** *101* (2-3), 157-170.

105. Madejova, J.; Komadel, P., Baseline studies of The Clay Minerals Society Source Clays: Infrared methods. *Clay Clay Miner* **2001,** *49* (5), 410-432.

106. Griffiths, P. R., Fourier-Transform Infrared Spectrometry. *Science* **1983,** *222* (4621), 297-302.

107. Gerwert, K.; Kötting, C., Fourier Transform Infrared (FTIR) Spectroscopy. *Encyclopedia of Life Sciences (ELS). John Wiley & Sons* **2010**.

108. Keller, K., Guidelines for Physicochemical Characterization of Biomaterials. NIH Publ.: 1980; pp. 80–2186.

109. Andrade, J. D., X-ray Photoelectron Spectroscopy (XPS). In *Surface and Interfacial Aspects of Biomedical Polymers*, 1985; pp 105-195.

110. Moulder, J. F.; Stickle, W. F.; Sobol, P. E.; Bomben, K. D., Handbook of X-ray Photoelectron Spectroscopy. In *A Reference Book of Standard Spectra for Identification and Interpretation of XPS Data* [Online] Physical Electronics, Inc.: Eden Prairie, Minnesota, 1995.

111. Owner, F., Fisitech. **2011**.

112. Macromolecular Crystallography Protocols. In *Structure Determination* [Online] Doublié, S., Ed. 2007.

113. Cullity, B. D., Elements of X-RAY DIFFRACTION. 1978.

114. Coats, A. W.; Redfern, J. P., Thermogravimetric Analysis. *Analyst* **1963,** *88* (105), 906-&.

115. Taninouchi, Y. K.; Uda, T.; Awakura, Y.; Ikeda, A.; Haile, S. M., Dehydration behavior of the superprotonic conductor CsH2PO4 at moderate temperatures: 230 to 260 degrees C. *J Mater Chem* **2007,** *17* (30), 3182-3189.

116. Revil, A.; Pezard, P. A.; Glover, P. W. J., Streaming potential in porous media 1. Theory of the zeta potential. *J Geophys Res-Sol Ea* **1999,** *104* (B9), 20021-20031.

117. Hunter, R. J., Zeta potential in colloid science: principles and applications. Academic press London: 1981.

118. Liese, A.; Hilterhaus, L., Evaluation of immobilized enzymes for industrial applications. *Chem Soc Rev* **2013,** *42* (15), 6236-6249.

119. Kirby, B. J.; Hasselbrink, E. F., Zeta potential of microfluidic substrates: 1. Theory, experimental techniques, and effects on separations. *Electrophoresis* **2004,** *25* (2), 187-202.

120. Obrien, R. W.; Midmore, B. R.; Lamb, A.; Hunter, R. J., Electroacoustic Studies of Moderately Concentrated Colloidal Suspensions. *Faraday Discuss* **1990,** *90*, 301-312.

121. Hanaor, D.; Michelazzi, M.; Leonelli, C.; Sorrell, C. C., The effects of carboxylic acids on the aqueous dispersion and electrophoretic deposition of ZrO2. *J Eur Ceram Soc* **2012,** *32* (1), 235-244.

122. Linge, K. L.; Jarvis, K. E., Quadrupole ICP-MS: Introduction to Instrumentation, Measurement Techniques and Analytical Capabilities. *Geostand Geoanal Res* **2009,** *33* (4), 445-467.

123. Bettmer, J.; Bayon, M. M.; Encinar, J. R.; Sanchez, M. L. F.; de la Campa, M. D. F.; Medel, A. S., The emerging role of ICP-MS in proteomic analysis. *J Proteomics* **2009,** *72* (6), 989-1005.

124. Rodriguez-Gonzalez, P.; Marchante-Gayon, J. M.; Alonso, J. I. G.; Sanz-Medel, A., Isotope dilution analysis for elemental speciation: A tutorial review. *Spectrochim Acta B* **2005,** *60* (2), 151-207.

125. Liu, X. H.; Ma, D. M.; Tang, H.; Tan, L.; Xie, Q. J.; Zhang, Y. Y.; Ma, M.; Yao, S. Z., Polyamidoamine Dendrimer and Oleic Acid-Functionalized Graphene as Biocompatible and Efficient Gene Delivery Vectors. *Acs Appl Mater Inter* **2014,** *6* (11), 8173-8183.

126. Lin, Y. C.; Cao, Y.; Jang, J. H.; Shu, C. M.; Webb, C.; Pan, W. P., The synthesis and characterization of graphene oxides based on a modified approach. *J Therm Anal Calorim* **2014,** *116* (3), 1249-1255.

127. Everhart, D. S.; Reilley, C. N., Chemical Derivatization in Electron-Spectroscopy for Chemical-Analysis of Surface Functional-Groups Introduced on Low-Density Polyethylene Film. *Anal Chem* **1981,** *53* (4), 665-676.

128. Ebrahim, A. M.; Rodriguez-Castellon, E.; Montenegro, J. M.; Bandosz, T. J., Effect of chemical heterogeneity on photoluminescence of graphite oxide treated with S-/N-containing modifiers. *Appl Surf Sci* **2015,** *332*, 272-280.

129. Ramanathan, T.; Fisher, F. T.; Ruoff, R. S.; Brinson, L. C., Amino-functionalized carbon nanotubes for binding to polymers and biological systems. *Chem Mater* **2005,** *17* (6), 1290-1295.

130. Li, N.; Wei, X. Y.; Mei, Z.; Xiong, X. L.; Chen, S. M.; Ye, M.; Ding, S. G., Synthesis and characterization of a novel polyamidoamine-cyclodextrin crosslinked copolymer. *Carbohyd Res* **2011,** *346* (13), 1721-1727.

131. Lerf, A.; He, H. Y.; Forster, M.; Klinowski, J., Structure of graphite oxide revisited. *J Phys Chem B* **1998,** *102* (23), 4477-4482.

132. Wang, G. C.; Yang, Z. Y.; Li, X. W.; Li, C. Z., Synthesis of poly(aniline-co-o-anisidine)-intercalated graphite oxide composite by delamination/reassembling method. *Carbon* **2005,** *43* (12), 2564-2570.

133. Yang, H. F.; Li, F. H.; Shan, C. S.; Han, D. X.; Zhang, Q. X.; Niu, L.; Ivaska, A., Covalent functionalization of chemically converted graphene sheets via silane and its reinforcement. *J Mater Chem* **2009,** *19* (26), 4632-4638.

134. Niu, Y. Z.; Lu, H. F.; Wang, D. X.; Yue, Y. Z.; Feng, S. Y., Synthesis of siloxane-based PAMAM dendrimers and luminescent properties of their lanthanide complexes. *J Organomet Chem* **2011,** *696* (2), 544-550.

135. Zheng, P.; Gao, L. X.; Sun, X. G.; Mei, S. G., The Thermolysis Behaviours of the First Generation Dendritic Polyamidoamine. *Iran Polym J* **2009,** *18* (3), 257-264.

136. Fu, Y.; Wang, J. Y.; Liu, Q. X.; Zeng, H. B., Water-dispersible magnetic nanoparticle-graphene oxide composites for selenium removal. *Carbon* **2014,** *77*, 710-721.

137. Ahalya, N.; Kanamadi, R. D.; Ramachandra, T. V., Biosorption of chromium (VI) from aqueous solutions by the husk of Bengal gram (Cicer arientinum). *Electron J Biotechn* **2005,** *8* (3).

138. Kadirvelu, K.; Namasivayam, C., Agricutural by-product as metal adsorbent: Sorption of lead(II) from aqueous solution onto coirpith carbon. *Environ Technol* **2000,** *21* (10), 1091-1097.

139. Yates, D. E.; Healy, T. W., Mechanism of Anion Adsorption at Ferric and Chromic Oxide - Water Interfaces. *J Colloid Interf Sci* **1975,** *52* (2), 222-228.

140. Cornell, R. M.; Schindler, P. W., Infrared Study of the Adsorption of Hydroxycarboxylic Acids on Alpha-Feooh and Amorphous Fe (Iii)Hydroxide. *Colloid Polym Sci* **1980,** *258* (10), 1171-1175.

141. Harrison, J. B.; Berkheiser, V. E., Anion Interactions with Freshly Prepared Hydrous Iron-Oxides. *Clay Clay Miner* **1982,** *30* (2), 97-102.

142. Balistrieri, L. S.; Chao, T. T., Selenium Adsorption by Goethite. *Soil Sci Soc Am J* **1987,** *51* (5), 1145-1151.

143. Duc, M.; Lefevre, G.; Fedoroff, M., Sorption of selenite ions on hematite. *J Colloid Interf Sci* **2006,** *298* (2), 556-563.

144. Martinez, M.; Gimenez, J.; de Pablo, J.; Rovira, M.; Duro, L., Sorption of selenium(IV) and selenium(VI) onto magnetite. *Appl Surf Sci* **2006,** *252* (10), 3767-3773.

145. Hayes, K. F.; Roe, A. L.; Brown, G. E.; Hodgson, K. O.; Leckie, J. O.; Parks, G. A., Insitu X-Ray Absorption Study of Surface Complexes - Selenium Oxyanions on Alpha-Feooh. *Science* **1987,** *238* (4828), 783-786.

146. Zhang, P. C.; Sparks, D. L., Kinetics of Selenate and Selenite Adsorption Desorption at the Goethite Water Interface. *Environ Sci Technol* **1990,** *24* (12), 1848-1856.

147. Xie, G. Q.; Xi, P. X.; Liu, H. Y.; Chen, F. J.; Huang, L.; Shi, Y. J.; Hou, F. P.; Zeng, Z. Z.; Shao, C. W.; Wang, J., A facile chemical method to produce superparamagnetic graphene oxide-Fe3O4 hybrid composite and its application in the removal of dyes from aqueous solution. *J Mater Chem* **2012,** *22* (3), 1033-1039.

148. Deng, H.; Li, X. L.; Peng, Q.; Wang, X.; Chen, J. P.; Li, Y. D., Monodisperse magnetic single-crystal ferrite microspheres. *Angew Chem Int Edit* **2005,** *44* (18), 2782-2785.

149. Hu, C. Z.; Chen, Q. X.; Chen, G. X.; Liu, H. J.; Qu, J. H., Removal of Se(IV) and Se(VI) from drinking water by coagulation. *Sep Purif Technol* **2015,** *142*, 65-70.

Appendix

The original data obtained by ICP-MS are listed in the following tables. The detection limit (DL) for selenium by ICP-MS is 0.002 ppm.

Appendix 1 Selenite concentration after adsorption using different generations (0-4) of PAMAM-GO as adsorbents. Adsorbents dosage 0.2 g L^{-1}, initial pH = 6, room temperature (25 °C), shaking rate 300 rpm, adsorption time 24 h.

Adsorbents	Initial selenium concentration (ppm)	Selenium concentration after adsorption (ppm)		
		Measurement 1	Measurement 2	Measurement 3
GO-G0	41.6	39.6	39.3	39.9
GO-G1	44.7	41.4	41.5	41.3
GO-G2	41.6	36.3	36.2	36.5
GO-G3	41.6	34.7	34.4	34.9
GO-G4	43.2	37.9	38.0	37.9

Appendix 2 Selenate concentration after adsorption using different generations (0-4) of PAMAM-GO as adsorbents. Adsorbents dosage 0.2 g L^{-1}, initial pH = 6, room temperature (25 °C), shaking rate 300 rpm, adsorption time 24 h.

Adsorbents	Initial selenium concentration (ppm)	Selenium concentration after adsorption (ppm)		
		Measurement 1	Measurement 2	Measurement 3
GO-G0	43.0	42.2	42.0	42.6
GO-G1	44.7	42.7	42.6	42.9
GO-G2	43.0	36.9	36.5	37.3
GO-G3	43.0	30.8	30.1	31.6
GO-G4	48.9	35.3	35.0	35.3

Appendix 3 Selenite concentration after adsorption on GO-G4 with different initial selenite concentration. GO-G4 dosage 0.2 g L^{-1}, initial pH = 6, room temperature (25 °C), shaking rate 300 rpm, adsorption time 24 h.

Initial selenium concentration (ppm)	Selenium concentration after adsorption (ppm)
70.7	64.2
57.9	52.6
43.2	37.9
21.4	19
13.4	11.1
1.09	0.875
0.530	0.419
0.214	0.165
0.110	0.0883
0.0601	0.0502

Appendix 4 Selenate concentration after adsorption on GO-G4 with different initial selenate concentration. GO-G4 dosage 0.2 g L^{-1}, initial pH = 6, room temperature (25 °C), shaking rate 300 rpm, adsorption time 24 h.

Initial selenium concentration (ppm)	Selenium concentration after adsorption (ppm)
82.3	67.14
66.0	51.12
48.9	35.34
30.9	19.92
15.0	5.4
1.0	0.435
0.491	0.184
0.199	0.0456
0.101	0.0282
0.0546	0.0134

Initial pH	Initial selenium concentration (ppm)	Selenium concentration after adsorption (ppm)		
		Measurement 1	Measurement 2	Measurement 3
3	43.2	35.4	34.7	35.2
4	43.2	35.6	35.7	35.7
5	43.2	36.9	35.9	36.6
6	43.2	37.9	38.0	37.9
7	43.2	39.5	39.5	39.4
8	43.2	40.6	40.6	40.6

Appendix 5 Effect of initial pH on selenite adsorption on GO-G4. GO-G4 dosage 0.2 g L^{-1}, initial selenite concentration ~ 40 ppm, room temperature (25 °C), shaking rate 300 rpm, adsorption time 24 h.

Initial pH	Initial selenium concentration (ppm)	Selenium concentration after adsorption (ppm)		
		Measurement 1	Measurement 2	Measurement 3
3	48.9	23.5	23.1	23.5
4	48.9	24.1	24.3	24.2
5	48.9	32.0	31.9	31.9
6	48.9	35.3	35.0	35.3
7	48.9	43.2	43.3	43.2
8	48.9	47.2	47.3	47.1

Appendix 6 Effect of initial pH on selenate adsorption on GO-G4. GO-G4 dosage 0.2 g L^{-1}, initial selenate concentration ~ 40 ppm, room temperature (25 °C), shaking rate 300 rpm, adsorption time 24 h.